Laser Surface Texturing for Novel Interference Fit Joint Fixation

A thesis Submitted for the Award of MEng

By

Solomon Ubani

School of Mechanical Engineering

Dublin City University

Supervisors

Prof. Dermot Brabazon

Dr. Muhannad Obeidi

September 2019

Declaration

I hereby certify that the material, which I now submit for assessment on the programme of study leading to the award of MEng is entirely my own work, and that I have exercised reasonable care to ensure that the work is original, and does not to the best of my knowledge breach any law of copyright, and has not been taken from the work of others save and to the extent that such work has been cited and acknowledged within the text of my work.

Signed: Solomon Ubani
ID No.: 15210076
Date: September, 2019

Acknowledgements

I would want to express my thanks to Prof. Dermot Brabazon for choosing the project on my Masters and his assistance in my research and my success on the course. I want to thank my supervisor Dr. Muhannad Obeidi for his contribution to all my research and his assistance in my research to make my masters successful.

I would like to send my thanks to Dublin City University for accepting me unto the course and for the training that I received for my research. I would want to thank Dr. Eanna Mccarthy who assisted in my course and for his contribution to my research.

I would want to thank the support from the technical staff in the School of Mechanical and Manufacturing Engineering, which are Liam Dominican, Jim Barry and Christopher Crouch for their assistance in providing materials for my research.

Table of Contents

Nomenclature

Symbols/Abbreviations (Constants)	*Description*	*Units*
PRF	pulse repetition frequency	Hz
d	beam diameter	mm
T	period	ms
λ	wavelength	μm
f	frequency	Hz
p	gas pressure	MPa
f	focal length	mm
d	pin diameter	mm
e	height of surface texture	mm
w	width of surface texture	mm
p_R	aspect ratio of the surface textures	mm/mm
l_R	length of the bonded joint	mm
e	height of surface texture	mm
w	width of surface texture	mm
t	thickness of the interference	mm
d_i	inner diameter of the hub	mm
d_o	outer diameter of the hub	mm
d	pin diameter	mm
t	thickness of the interference	mm
t	thickness of the interference	mm

Symbols/Abbreviations (Variables)	*Description*	*Units*
z_f	focal position	mm
O. V	percentage overlap	%
v_s	scanning speed	mm/min
V_f	transverse speed	mm/min
V_t	tangential speed	mm/min
H	spacing distance	mm
d_{min}	minimum spot size	mm
w_o	laser beam radius	mm
$w(z)$	beam radius depends on depth of focus	mm
r	laser spot size	mm
P_A	laser beams amplitude	W
P_L	laser power	W
τ	pulse duration	ms
w	laser beam intensity	MW/m^2
E_d	laser energy density	J/mm^2
I	laser irradiation density	kW/mm^2
E_d	fluence	J/mm^2
E_o	pulse energy	J
T	Surface temperature	ºK
t	residence time	ms
$\dot{T}$	cooling rate	°K/s
V_A	austenitic fraction	%
V_M	martensitic fraction	%
V_H	heating rate	°K/s

δ	strain	mm/mm
Ra	surface roughness	μm
RSm	peak-to-peak width	μm
Rc	peak to valley depth	μm
F_a	insertion force	kN
F_n	pull-out force	kN
F	joint force	kN

List of Tables

List of Figures

List of Papers

This thesis describes original submitted work for a degree in Dublin City University. The investigation was carried out in the School of Mechanical Engineering for the award of MEng. This work has disseminated into publications, abstracts and seminars.

Journal Papers:

Ubani, S., Obeidi. M and Brabazon, D. (2019), "Laser surface texturing for the improvement of press-fit joint bond strength" AIP Conference Proceedings, 2113, (150013).

Seminar, Abstract:

Ubani, S. (2019) 'Laser scanning method for the improvement of the surface morphology, grain size, contact area of interference bonded joints' [PowerPoint], Research Day Presentation.

Ubani, S., Obeidi, M. and Brabazon, D. (2018) 'Laser Surface Texturing for Novel Interference Fit Joint Fixation', EasyChair: AMPT2018 Conference

Abstract

Laser Surface Texturing for Novel Interference Fit Joint Fixation

Solomon Ubani

In this project, a new type of manufactured interference fit joint was examined. Interference fit joints hold components together in many industries, including the automotive, ICT, and aerospace industries. The interference fit joint consists of a pin and a hub region. As the rod is inserted into the hub, deformation of the material results in a joint bond strength. Laser surface texturing of metal pins for was used for manufacture of interference fit joints. The material examined was mild steel EN3B, a carbon steel with a difficult to machine and has high melting point. The laser parameters investigated in this study were the laser power, the laser scan percentage overlap and the focal position. These have significant effects on the resulting surface texture geometry. The peak-to-valley and peak-to-peak displacements can be controlled using the laser. The process obtained different surface geometries such as groove or moiré stochastic structures. The process parameters and their levels were used to alter the specific volume of material raised above the pin surface. Higher volumes characteristics resulted in larger interference fit joint bond strengths. The laser parameters obtained surface textures as well as on the various dimensions of melt pool volume, grain sizes and diameter increase of the pin of the joint. The phase transformations also resulted in various microstructure properties on the samples. The interference fit pin was 60 mm in length and 9.8 mm in diameter. Surface textures were produced on the engagement length of 10 mm along the length of the pin. The results of the investigation obtained a range of textured diameter increases from 10mm to 10.8mm and surface roughness from 38.8μm to 92.7μm. The insertion force values were between 0.91kN and 29.4kN and pull-out force values were between 0.15kN and 7.81kN. The process parameters which were the most significant for the diameter increase where the laser power and the percentage overlap of the laser spot. The surface roughness had a significant correlation with the focal position and the laser power on the specimen. The interference-fit joints achieved joints that safer compared with conventional interference fit joint. This was due to the fact that the bond strengths of joints had lower 95% error bars of the specimens. These joints also exhibited re-grip on excess loads compared with the traditional interference fit joint used in the automotive manufacturing industry.

Chapter 1

Laser Processing of Materials

1.1 Introduction

Laser surface texturing is a commonly used method of surface treatment. This process has many benefits compared to current traditional methods of machining of materials. In the literature, there are investigations into applications for development of surface textures for a variety of purposes. However, there is lack of research for interference fit joints.

Laser surface textures are used in applications such as cylinder liners and piston rings [1]. These components require a high load carrying capacity. This involves low friction contact surfaces for improvement of energy conversion and minimization of heat losses. Research in the use of this process can have many benefits to manufacturers in high volume processes, assembly, and disassembly and repair of components. Investigations of the process will enhance the efficiency of the operation of vehicles.

In the manufacturing sectors, steel materials in transport and structural design must meet safety and performance requirements. High mechanical strength is needed for many interference fit applications. Improvement of surface properties of metals can lead to broader range of applications. These include highly efficient energy conversion in transport vehicles and reduction of emissions of most vehicles.

Obeidi *et al*. [2] reported that the laser micro-surface processing in the formation of a variety of surface texture geometries. Laser surface textured metals results in surface features for an improved lifetime due to surface finish and quality of joints. Surface textures also result in improvement on the joining forces for fixation of the pin and hub components for interference fit purposes. Press-fit as a joining method can obtain high joint strength and facilitate assembly and disassembly processes. Previous research of laser surface texturing has found further benefits of the laser process on surface quality of the parts. Laser surface textures improves to not only improve strength but prolong the service time of the parts. This is through the development of pin specimens that even after failure regrip the joint [2].

This process is beginning to gain more uses in the industry compared to other surface modification methods [3, 4]. Recent investigations of process parameters to produce surface textures has led to further improvements, for example improved hardness and examination of plastic deformations where the yield strength of the material is exceeded [5]. There is significant attention toward being able to precisely control the forces at the interface.

This research project was focussed on developing an improved interference fit joint via laser surface texturing. The results showed that a high level of control can be achieved over the surface texture geometry and resulting interference fit bond strengths.

1.2 Background of Project

Laser melting transforms the melted region of the surface into the required surface texture. Laser surface texturing manufactures interference fit joints with textures of definable peak to valley heights and peak-to-peak widths. The laser processing method creates interference by the formation of pins with larger diameter and tight tolerances between the hub joint. This pin is then fitted into a smaller diameter hub which produces an interference.

According to Gibson and Shi [6], the conditions of process measured and related to the performance of the process. The responses include surface temperature, laser surface intensity, temperature gradient of the material [7]. The substrate temperature before and during laser surface texturing is known to affect the resultant joint strength.

In the literature, heat treatment of materials below the melting temperature can result in changes of the surface properties [8]. Laser melting at and above the melting temperature and subsequent solidification affects the strain rate of deformation during assembly and disassembly of the joints [9]. This gives different characteristics of the load-extension curves [10]. According to Katayama *et al*., the external loads can act on the pin and hub assembly. This contributes to failure of the joint when in service. This particularly occurs when pins and hubs of tight dimensional tolerance are utilised [10, 11, 12]. Specimens can have different degrees of plastic deformation dependant on different pin diameters of the joint [13]. The level of interference has the main impact on the process of deformation of the surface textures on the parts. Process parameters can be used to vary the dimensions such as the width and depth of the melt pools on the specimens.

1.3 Statement of Research Investigation

From past published articles, there is a lack of detailed examination of how the process parameters affect the laser surface texture and achievable interference fit bond

strengths [2]. Interference fit dimensions e.g the engagement area affect bond strength of the material. Surface textures that are consistent reduce interfering volume and reduce the level of assembly forces required [10]. Laser surface textures that produce large length scales are porous in structure. This can aid in the assembly of parts due to lower levels of interfering forces based contact area between the pairs of mating parts [14]. Development of press-fit parts in the automotive industry, often results machined parts that have inconsistent surface roughness topography of the specimens. This is an important consideration to effectively produce considerable increase in bond strength of the specimens. Investigations into laser surface textures is due excessive melting processes affecting repeatability and control over these surface textures of these interference fit applications.

1.4 Summary

In this study, laser processing parameters effects resulting surface finish and quality characteristics of the specimens was examined. This investigation involved production of clearly defined micro-surface textures of different structures over the surfaces of cylindrical geometries made of steel. The melt surface and its relationship to the processing parameters was examined. The geometry of the surface textures obtained high roughness values on the pins. These were used in specimen characterization of surface properties. The experiments obtained different depths and widths of the grooves on the pin. In this project, the specimens these melt pool dimensions resulted in different ranges of assembly forces at the interface and surface qualities due to plastic deformations of the pin in the hub joints.

Chapter 2

Literature Review

2.1 Steel Properties

Steel alloy properties have high strength that make it a good material choice for various applications and production methods. Steels such as carbon steels contain a variety of elements that include Mn, Si, Ni, Cu, Cr, Mo, V, and W. This give it a range of unique properties in interference fit applications. In the literature, the surface processing of steel affects this surface elemental composition. In the automotive industry, materials such as alloy steels are used because it is formable and possesses useful mechanical properties. Carbon steel is used by researchers for investigation due to its the high tensile strength. This makes suitable for laser manufacturing due to its relatively low embrittlement of the material.

Figure 2-1 shows the phase diagram of steel compositions. This shows phase states and the carbon contents at different temperatures [15].

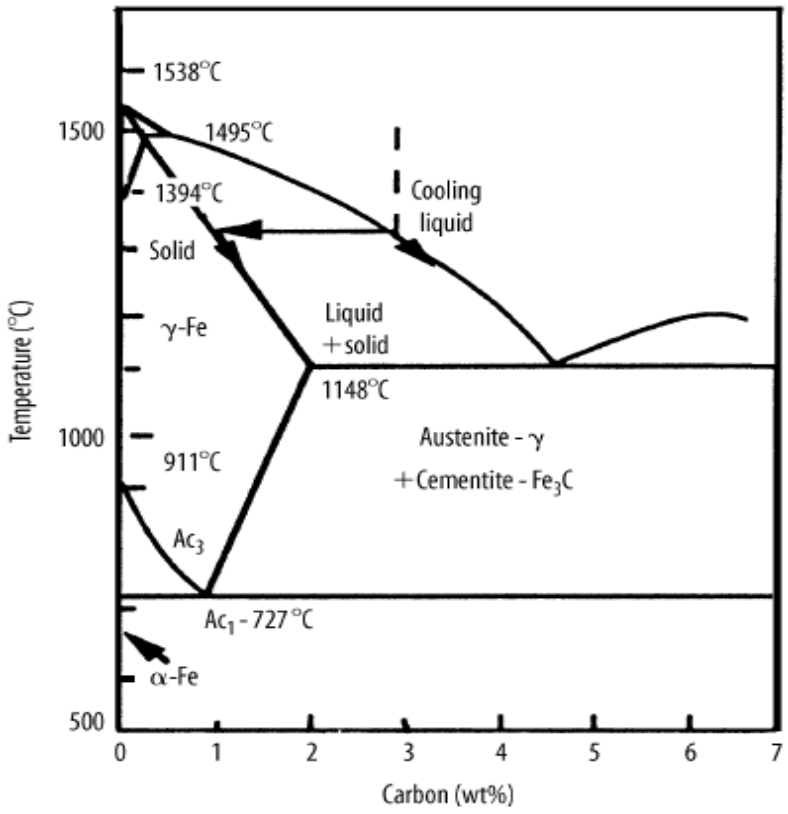

Figure 2-1: Fe-C phase diagram showing phase variation with temperature and % C [16].

2.1.1 Steel Properties

Steels have different categories of microstructure properties and chemical compositions including 1. Cementite Steels, 2. Pearlite Steels, 3. Martensite Steels, and 4. Ferrite Steels.

Cementite Steels

Cementite steel, noted as γ phase, has an Hexagonal Close Packed (HCP) structure which has high strength properties. Cementite steels Fe_3C, have high cost of manufacture due to the high heating temperatures of the process. As well as being strong, cementite is also very hard and brittle. Cementite steels can contain Molybdenum, Silicon, Manganese and Nickel.

Ferrite Steels

Ferrite steels have an α phase grain structure that is Body Centred Cubic (BCC) and is a relatively soft phase. The as received state of steels is often in the form of ferrite to allow for the easy manufacturing of parts.

Pearlite Steels

Pearlite steels have a combination of α and γ phase produced upon cooling from the molten material. The microstructure has an Face Centred cubic (FCC) atomic structure. Pearlite is made up of fine particles of ferrite and iron carbide content. This gives the strength of the metal. Pearlite steels have higher ductility than other steels phase types.

Martensite Steels

Martensite steels have a chemical composition of β phase with a Body Centre Cubic (BCC) microstructure. This microstructure provides a high strength. Martensite has a fine structure. This results from rapid cooling, that is very hard. The phase has an intergranular structure that gives the macroscale high strength properties.

2.1.2 Steel Types

Steels are alloys of Fe and C and there are different types such as plain carbon steel with less than 2% carbon, low alloy steel, high alloy steel and stainless steels metals. There are various classifications of steel such as AISI and DIN [17]. The steel types and there percentage compositions can be classified according to their carbon content below:

Plain Carbon Steel

Carbon steel has the lowest cost of manufacture. This is the most commonly used steel for many different applications in the industry. The microstructure can be classified into the subgroups which are low Carbon (less than 0.3% carbon), Medium carbon (0.3% to 0.6%) and High carbon (0.6% to 0.95%) metals [17]. During its manufacture, if the carbon is greater than 0.6%, quenched hardened austenite steel is produced from the process. Carbon steels commonly used have designation from 1006 to 1050 for manufacture processes. The properies of different types of plain carbon steel and examples of typical metals are given below [18]:

a) Low Carbon: This microstructure has less than 0.3% Carbon composition. Typical metals include AISI 1008, 1010, 1015, 1018, 1020, 1022, 1025 for the machining processes.
b) Medium Carbon: This microstructure has a Carbon content between 0.3% to 0.6% compositon. Commonly used metals are AISI 1030, 1040, 1050, 1060 for manufacturing processes.
c) High Carbon: This microstructure has a compositon of 0.6% to 0.95% Carbon content. Commonly metals used are AISI 1080, 1095 for manufacture.

Alloy Steel

Alloy steels are steels that other alloying elements along with Iron and Carbon content. This gives it benefits over plain carbon steels e.g. improvement of physical properties and manufacture of the material. These alloying elements include Sulphur, Phosphorous and Lead content. These elements aid the ease of manufacture of the metal. Alloy steels can be categorised into the following types: low, medium and high alloy steels. Low alloy steels contain less than 5% of the additional elements. Medium carbon steel contains between 5% and 20% content. High alloy steels e.g. stainless steel have greater than 20% of other elements [18].

2.1.3 Microstructure Properties of Steel

Studies of laser processing of materials have shown that the impact of residence time on the rate of cooling of the component. The rate of heating and cooling are important factors that result in particle arrangement and hence the microstructure of the part [19, 20]. In previously published papers, it was found that high residence times had surface textures that

are fine crystalline structure. In other results low residence times produced a coarse amorphous microstructure on the samples [21].

Alloy steels that are know as high strength steels e.g. Stainless steel 316L has a high melting temperature of 1,723°K. The shielding gas cooling from this temperature can give a range of microstructures and surface properties. Laser processing and subsequent solidification of more than 10^3K/s gives a much finer grain microstructure and below a much coarser structure on the material surface [3]. The process parameters determine this rate of solidification and resultant material microstructure. Dhahri *et al*. [14] reported that the laser surface treatment can increase the extent of dendrites in the material. This gives it a much denser and grain size of the metal

2.1.4 Phase Composition of Steel

Vasumathy *et al*. [19] reported that austenitic stainless steels 316L has to fine grains. This phase microstructure gives it high strength and toughness in comparison to the martensitic and ferrite phase formation of the steel [22]. Therefore, austenitic steel phase has a much higher insertion forces during interference fit assemblies. Additional steel property include the tribological properties of the material. In research, it was found that carbon steels have lower cohesive forces that alloy steels between the particle. This steel property results in a much higher diameter increase due to laser melting and solidification of molten material. The processes of heating is also known to increase the carbon content in the metal. This is useful in the development of the meltpool and higher carbon content reduces the binding energy between the parts. The application of the laser parameters results in higher depth and spacing distance between the surface textures on the material.

2.2 Laser Surface Texturing Process

The process parameters control the thermal input and melting process. Laser parameters that have the main effect include laser beam power, P, pulse repetition frequency, PRF, and percentage overlap, O.V [2]. In previous studies, an example of laser process parameter settings used in experiments of CO_2 laser testing of stainless steel is shown in Table 2-1.

Table 2-1: CO_2 laser processing parameters used for surface texturing [2].

Sample no.	Power (W)	PRF (Hz)	Overlap (%OV)	ω (rpm)	V_L (mm/min)
Ov-1	500	300	0	71.6	14
Ov-2	500	300	20	59.68	10
Ov-3	500	300	-20	89.5	21

Surface textures with different percentage overlaps i.e. the percentage amount between adjacent surfaces textures on the specimen. This overlap of scanning tracks provides different surface roughness on the samples. In research, components in machining process investigated had cylindrical geometry. These are used because of ease of machining and distribution of haexagonal pattern across the surface of the specimen. These testing process as interference fit parts are usually of axisymmetric shaped geometry [3]. In that project, peak to valley depths and peak-to-peak widths were surface textured between cavities on the samples. The process was achieved by melting a surface volume on the specimen. The re-solidified molten metal forms an increase in the pin diameter. This increase is essential for the interference-fit (press fit) application. Surface textures with a wide range of geometries were obtained from dimples to columnar and Moiré type structures. These depend on the laser operation but there is a lack of methodology or process maps for the manufacture of readily achieved for such joints.

2.2.1 Laser Surface Modification Process

In experimental studies, Vladescu *et al*. [1] reported interference fit applications such as piston rings moving in cylinder liners. These were surface textured for improvement of sliding motion between the parts. The authors obtained periodic surface texture geometries between adjacent surfaces of parts. The experiment found that pillared structures on cylinder liners with lubrication had a significant engagement area on the reciprocating parts. Shum *et al*. [23] reported a laser formation of surface geometries on parts. The author also obtained surface textures can be in the form of dimples, Moiré, and pillars structures geometries on the specimens.

Laser micromachining of materials involves laser beam production of the phase change at the surface of the components [24]. According to Poprawe [3], laser irradiation produces melting and cooling at different rates on the surface. Laser surface modification

depends on the laser intensity (absorbed power density) and interaction time on the components. Commercial lasers that have short pulse length produce surface structures at length scales of micrometres and nanometres in size on specimen [25]. Laser processes can produce surface textures of a wide range of chemical properties and tribological properties [26]. These are formed at various thermal input transferred to the bulk material of the specimens.

2.3 Laser Parameters

According to Roy *et al*. [27], performed laser surface heat treatment with a CNC controlled continuous wave CO_2 laser on a positioning stage. The author reported that various methods of formation of slightly higher surface roughness (e.g. to 3 μm Ra). This was performed due to higher laser energy surface absorption on the specimen [28]. Surface treatments that result in this effect include etching, pitting, and blasting. Ponce *et al*. [22] studied surface treatments for removal of surface layers. This improved the application of the laser beam of the component. Laser surface process produces a melt pool depth that depends on the translational speed underneath the laser spot. The melt pool depth, δ, can be calculated from the rotational speed, N and thermal conductivity of the metal workpiece, K below [3];

$$\delta = \sqrt{\frac{2}{N\pi K}} \tag{2-1}$$

2.3.1 Laser Wavelength

The wavelengths of lasers used for material processing are shown in the Table 2-2. Lasers that have a shorter wavelength generally process more efficiently metallic surfaces.

Table 2-2: Wavelengths of different lasers [16].

Laser Type	Wavelength, λ (μm)
Argon	0.488
He-Ne	0.6328
Nd: YAG	1.06
CO	5.4
CO_2	10.6

2.3.2 Pulse Repetition Frequency

Lasers can operate at different pulse repetition frequency, PRF. This can be controlled to define the number of pulses impingement on the sample. The pulse duration can be represented as the spot diameter, d, divided by the spot scan speed above the specimen. Pulse repetition frequency, PRF is defined as the inverse of the period. As given by equations 2-2 and 2-3 respectively below:

$$\text{Pulse duration}, \tau = \frac{\mathrm{d}}{V} \tag{2-2}$$

$$\text{Pulse repetition frequency}, \mathrm{PRF} = \frac{1}{\mathrm{Period}} \tag{2-3}$$

Table 2-3 shows the pulse wave parameters of some commercial lasers. This includes the fundamental frequency, f and wavelength, λ of the lasers [29].

Table 2-3: Fundamental frequency range of lasers used for processing materials [16].

Laser	Wavelength (μm)	Fundamental frequency range, (MHz)	Cavity length (mm)	Number of modes
He-Ne	0.6328	1700	1000	10
Argon	0.50125	3500	1000	20
CO_2	10.6	3000	1000	20
Nd: YAG	1.06	6000	100	40

Pulse duration is a parameter varies with the energy density applied on the sample. This parameter changes the depth of the grooves on the specimen. The increase in pulse duration results in larger depths [16, 25].

2.3.3 Laser Percentage Overlap

Surface modification parameters that affect the groove dimensions and spacing of surface textures. The main parameters include spot scan speed, v, and laser spot diameter, d, on the material [30]. The situation of laser processing of a pin geometry involves rotation

and axial translation of the specimen. This scanning method is in order for the laser spot to distribute laser scanning tracks evenly on the pin specimen. For a pin of diameter D and rotational speed N, described that the laser beam speed along the surface in the tangential direction below (Kothandaraman and Rudramoorthy [10]):

$$\mathrm{v_t} = \frac{\pi\, \mathrm{D}\, N}{60} \tag{2-4}$$

Laser traverse speed in the longitudinal direction can be calculated according to the relationship below:

$$\mathrm{v_f} = \mathrm{d} \times \mathrm{N} \times (1 - \mathrm{O.V}) \tag{2-5}$$

Bartkowska *et al*. [30] reported that the distance between the grooves and laser spot diameter expressed as the percentage overlap of the sample. The laser scanning speed, v is the resultant of the laser tangential speed, v_t and the laser traverse speed, v_f of the laser during the process. The laser scanning speed, v, can be calculated as follows:

$$v = \sqrt{{v_f}^2 + {v_t}^2} \tag{2-6}$$

The laser scanning method consists of a variable translational speed and rotational speed on the workpiece [31]. This creates grooves of various angles and geometries on the circumference of the work piece.

According to Obeidi et al. [2] the percentage overlap can be represented in terms of the PRF, rotational speed, ω, the spot size, d and diameter of the workpiece below:

$$\mathrm{O.V} = \left[\frac{PRF \times 60 \times d}{\pi \times D \times \omega} - 1\right] \times 100\% \tag{2-7}$$

This can be written in terms of the translational speed of the laser beam in the axial direction on the workpiece in the equation below [2]:

$$\mathrm{V_L} = d \times \omega \times (1 - O.V) \tag{2-8}$$

The percentage overlap, O.V, of the spots result in the formation of surface textures of different widths and positions on specimen. Figure 2-2 shows a surface texture geometry with peak-to-peak widths and the peak to valley depths of the surface textures on specimens [2, 32].

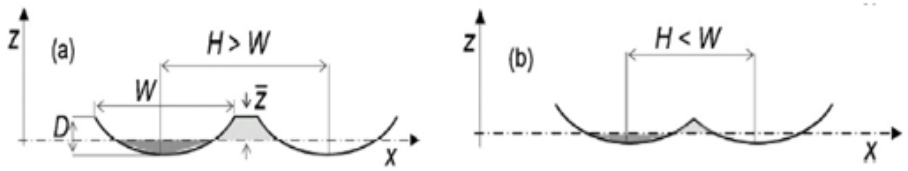

(a) (b)

Figure 2-2: Schematic of overlap of surface textures for (a) H > W, and (b) H < W on the surface of the samples [33].

2.3.4 Laser Power

The laser power, P, can be defined as the laser energy supplied to the material for a specific pulse repetition frequency. The equation of the laser power is given below:

$$P = \frac{\mathrm{E}}{\mathrm{PRF}} \tag{2-9}$$

The laser power density is the ratio of the power applied to the surface area of the workpiece during the laser surface texturing process. The power density is known as the irradiance, I on the specimen.

2.3.5 Laser Mode

Laser pulse mode is a parameter that affects the melt depth of the process. This can be used to vary the distribution of pulses on the material. There are two types of laser modes that determine the wave structure of the laser beam below [16, 34].

1. Continuous Wave Propagation: This laser mode has a higher spatial and temporal consistency. This gives it a high depth of processing into the material. With this laser mode lower energy is used to process a given volume of the workpiece. This wave propagation is suitable for drilling, cutting, and machining of specimens.
2. Pulse Wave Propagation: This laser mode has a lower temporal consistency due to its dependence on pulses and changes in frequency. This propagation gives it a more refined control of the depth of the process on the surface of the material. This mode of wave propagation is suitable for polishing, surface texturing and heat treatment of materials.

2.3.6 Laser Focal Position

The focal position is defined as the height of the objective of the laser above the workpiece. This is the position of the laser that focusses the laser beam on the sample. This laser results in a laser spot radius of w(z) that is a function of the focal position from the

initial spot radius of w_o on the material. Lasers have a spot radius that is related to the focal position and spot diameter as shown below [16]:

$$w^2(z) = {w_o}^2 \left[1 + \left(\frac{\lambda z_f}{\pi {w_o}^2}\right)^2\right] \quad (2\text{-}10)$$

where w(z) is the spot radius that depends on focal position, w_o is the initial beam radius, and λ is the wavelength of the laser. Figure 2-3 shows this schematically.

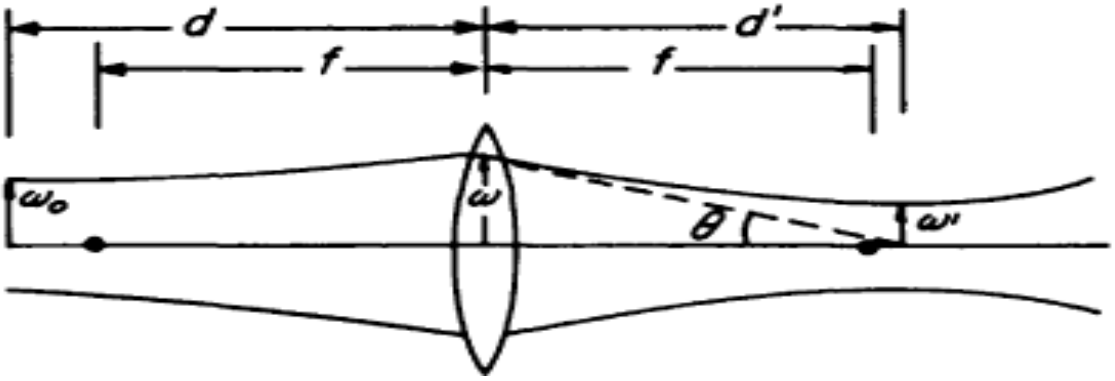

Figure 2-3: Experimental schematic of focusing of the laser beam on the surface of the material [31].

The process parameters that can be adjusted before the process are the focal position and resultant spot size. These parameters contribute to the resultant surface texture dimensions.

2.3.7 Laser Spot Size

Spadaro *et al*. [35] reported that the spot size affects the laser power density and surface structures geometries. For the circular beam at the wavelength, λ, focal length, f and beam diameter, B, results in minimum spot size in the equation as follows:

$$d_{min} = 2.44 f\lambda / B \quad (2\text{-}11)$$

2.3.8 Laser Spot Radius

The laser spot radius, w_o can be calculated for a Gaussian distribution in the equation shown below [16]:

$$w_o = \frac{2\lambda f}{B} \quad (2\text{-}12)$$

where λ is the wavelength of the laser radiation, f is the focal length of the objective, B is the beam diameter of the objective of the laser, and w_o is the laser spot radius. The laser spot size can be related to the laser beam diameter in the equation below [16]:

$$\frac{f}{z_f} = \frac{B}{d_{min}} \tag{2-13}$$

$$d_{min} = \frac{z_f B}{f} \tag{2-13}$$

where f is the focal length, B is the beam diameter, d_{min} is the spot size and z_f the focal position above or below the sample surface. The laser spot size can adjust depending on the distant between the laser nozzle and samples surface.

2.3.9 Laser Assist Gas Composition

According to results of Peng et al. [36], the composition of the assist gas affects the quality of the laser micromachined material. A laser with an assist inert gas flow reduces oxidation due to the avoidance of oxygen from the surrounding atmosphere on the specimen. A sample in the presence of high temperatures would otherwise react with the oxygen to form an oxide layer. Therefore, inert gas atmosphere e.g. nitrogen or argon are used for stainless steel 316L. An example of laser processing with an inert gas is shown in Figure 2-4 [37].

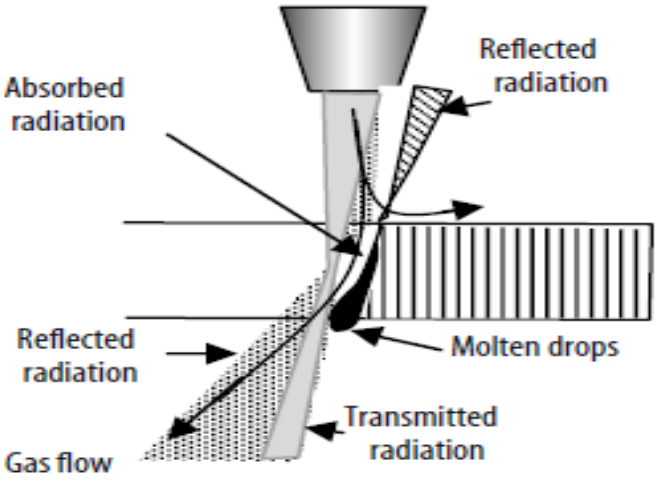

Figure 2-4: Schematic of laser material processing with inert gas [16].

2.3.10 Pulse Energy

In laser manufacturing processes, the laser energy density depends on the laser power on the surface of the specimen. The laser energy density, E_d used during the process and the process parameters can be related for a given surface area of the workpiece as [31, 38]:

$$h = d\left(1 - \frac{O.V}{100}\right) \tag{2-14}$$

$$E_d = \frac{P}{Vht} \tag{2-15}$$

where d is the laser spot size, O.V is the pulse overlap, P is the laser power, h is the spacing distance, V is the laser scanning speed above the workpiece and t is residence time. In the equation, h is defined as the distance between the consecutive peaks or valleys of the surface textures on the substrate surface. The laser process produces a uniform distribution of hexagonal arrangement of laser pulses on the specimen Romano et al [39].

2.3.11 Residence Time

The laser residence time is the time the laser energy is supplied to the surface before cooling with the assist gas to the specimen Chikarakara *et al* [40]. According to Kumar *et al*. [41], the residence time, t calculated in the equation shown below:

$$\mathrm{t} = \frac{\mathrm{d}}{\mathrm{v}} \tag{2-16}$$

2.4 Factorial Design

Factorial design of experiments is a method used to examine the process parameters (also called factors) to the output responses. In this method, the effects of the variable parameters and their levels as well as their interactions can be assessed. In the method, the experiments are performed with different combinations at "k" number of levels and "n" number of parameter [42]. 'DesignExper't is a software package that enables examination of experimental inputs and outputs according to the Design of Experiments (DOE) or Response Surface Methodology.

The polynomial correlation is found using the least squares and step-wise regression of the significant factors at 95% confidence interval ($\alpha = 0.05$) in order of fit of the results. This is given by the formula below with the error between experiments and model, ε of in the equation below:

$$y = f(x_1, x_2, \dots, x_k) + \varepsilon \tag{2-17}$$

where k is the number of variables used for the laser surface texturing experiment. This response surface method can be run as two-level, full or fractional factorial points (2^k or 2^{k-1}) for a central composite design (CCD) to provide predictions of the design space.

This factorial analysis runs with center points that are replicates of number of runs or the factorial design.

1) Replicated center points measure pure error for the lack of fit test. A lack of fit shows close the model fits the data.
2) For a block the central composite design the design is desirable. Block orthogonality is independent of the effects of the factors. Reducing the number of centre points will adversely affect these properties.
3) The number of centre points gives an almost uniform precision designs. Results with fewer the number of centre points increase the error in the design space.

To ensure that the design space are accurately modelled with the replicates, the number of centre points. This ensures that the analysis of the design can be performed with the model of the factors. The model of design space predicts the effects of the factors on the response. A Gaussian beam the process is modelled with a smooth curve of the data and minimum error that is orthogonal of the parameters. This should be used in the fractional factorial experiment and full factorial of odd number factors

2.5 Average Surface Roughness

The surface roughness depends on the translation speed and the cutting radius i.e (diameter increase/2) of the laser microsurface process. This relation was determined for machining process. It is accurate representation of the laser microsurface processing [41].

The measurements were subsequently calculated for the surface roughness of the samples [43]. The process was repeated three times for the average surface roughness and confidence intervals of the specimens. The equation for the average surface roughness of the material is given below:

$$s = v_f \times N \tag{2-18}$$

$$Ra = 0.321\left(\frac{s^2}{r}\right) \tag{2-19}$$

where *s* is the scanning rate and r is the radius of the cylindrical bar used for the laser surface texturing experiment.

2.6 Interference Fit Joints

Structural designs in the transport and manufacturing industry involve numerous parts assembled of different complex geometries. Research has led to new joining methods because of the precision and load carrying capacities of these parts [44]. Parts can have a range of size and strength requirements according to specific design requirements. The

interference fit parts operate in severe conditions. Therefore, it is required for functions e.g. prevention of leakage of piston cylinders, bearings, and seals in automotive applications. Therefore, interference fit parts require a high sealing performance for a long service life [12, 15]. Figure 2-5 shows interference fit parts used for sealing of viscous substances [45].

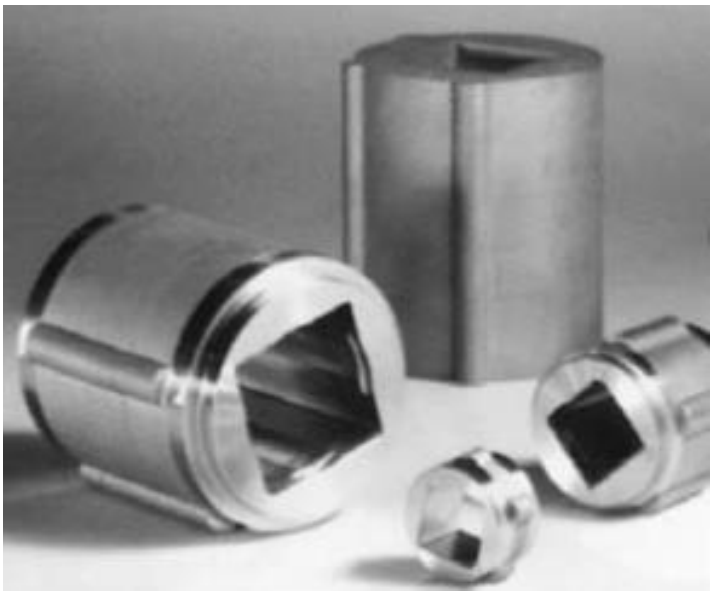

Figure 2-5: Stainless steel rotor hubs used for sealing of viscous substances [46].

Figure 2-6 shows the joined parts consist of flanges made of wrought steel 410 for gas sealing. These facilitate maintenance and are low in cost to produce in the transport industry. They operate at both atmospheric and high temperature for seals of gas for vessel applications. These parts are made with low interference values in the range of micrometres to nanometres. The sensor rings were manufactured from wrought stainless steel 410L and 434L. The interference fit joints during the insertion of a pin into the hub joint can result in damage of the hub material. Laser processed parts with an outer layer of oxides minimise the effect on press fit rings on the shafts in vehicles [46].

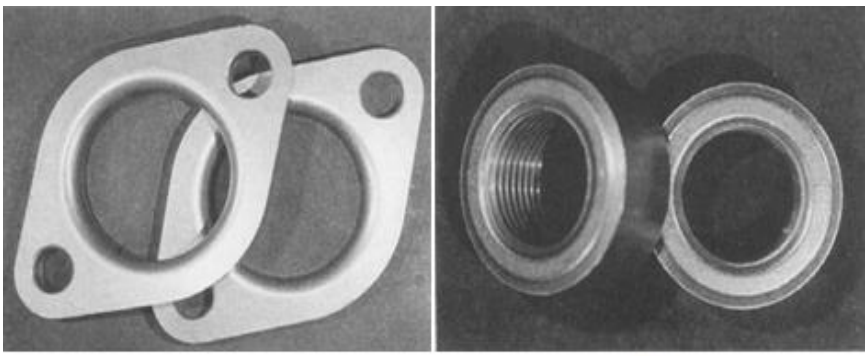

Figure 2-6: Wrought steel (a) flanges and (b) sensor rings using for sealing within of structural parts [46].

2.6.1 Interference Joining of Pin and Hub Components

The interference joining method requires no adhesive, solvent and fasteners and is a cost-effective method of assembly. The method of joining consists of snap and press fit types [47, 48, 49, 50]:

(a) Snap-fit: The snap-fit assembly is used for high volume manufacture of components without any disassembly of the components. In the snap-fit designs, parts of the moulded-in joining method bend for interference between the component. This is performed when it is position before assembly of the components.

Figure 2-7 below shows the snap-fit parameters including beam length, L, beam height, h, undercut depth, Y, insertion angle, α, the retention angle, β and the radius, R on the surface of the joint.

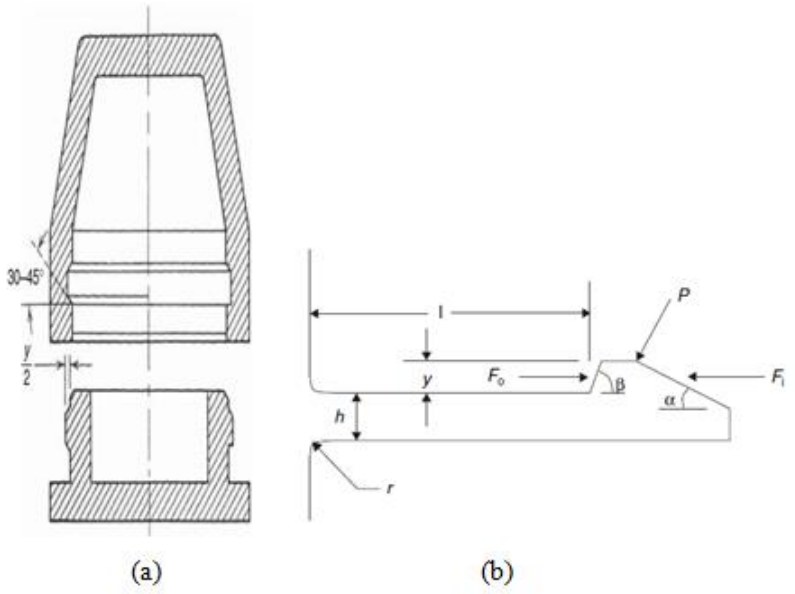

Figure 2-7: Snap-fit schematic of the (a) annular and (b) cantilever designs of components and the dimensional parameters [51].

(b) Press-fit: Press-fit joints interference to ensures the assembly of the parts. Due to the high loads required, the method of assembly can fracture of the components during the fixation of the shaft into the hub joint. Figure 2-8 below shows the press-fit to produce interference between the outer diameter of the shaft and the inner diameter of the hub of the joint.

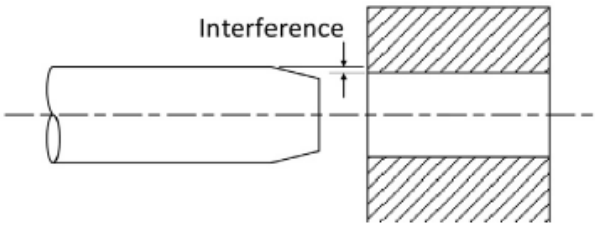

Figure 2-8: Press-fit schematic of the components and parameters of the joint [51].

2.7 Insertion and Pull-out Forces

The joint force of a pin inserted into a hub assumes a negligible diameter and a infinitesimal length e.g. a copper wire. This models the behaviour of micro-surface textures at the interface of pin and hub joint similar to a copper wire. From initial results of experiment by the author Ubani et al [52]. This approximation relates to theoretical results of previous research. The equation given by the author for a copper wire is given below composed of the side and lower surfaces of the cylindrical joint [53, 54].

$$F_{max} = \frac{\pi d^2}{4}\rho_R \sigma_f + \pi d l_R \tau_R \quad (2\text{-}20)$$

where σ_f is the tensile strength, τ_f is the shear interface strength, d is the diameter, p_R is the ratio of actual bonded area and the total lower surface area and l_R is the actual bond length of the specimen. The actual bond length is represented in terms of insertion and removal length. These are the incremental distances the pin moves during assembly and disassembly with the hub joint.

The interference fit joint produce fixation of the pin in the hub, F_a, axial force (insertion length) and F_n, normal force (removal length) on the interference fit pin. The joint force, F, for grooves of height, e, and width, c, of surface textures is calculated in the equations below [53].

$$p_R = \frac{e}{c} \quad (2\text{-}21)$$

$$F = p_R F_a + F_n \quad (2\text{-}22)$$

2.8 Steel Applications of Interference Fit Joints

Steels used for products in commercial applications have high strength and durability of the components. For commercial applications steel materials often have comparable mechanical properties to e.g. stainless steel alloys 304 and 439 types of wrought steels. The joints can withstand deformations. These joints when properly utilised prevent crack formation of the material [52].

2.9 Summary

As shown in Table 2-4, laser proceses are used wide variety of surface texturing applications. The purpose of the study was to understand the effects of laser texturing process parameters on the resultant interference press-fit joint of mild steel samples. Specifically, this work determines the effects of process parameters on the surface profile of mild steel EN3B. The resultant textures can be related to the optimum performance interference fits joints of textured pins.

Table 2-4: Micro-manufacturing performance varies surface textures sizes and process rates of materials [38].

Process	Principle	Minimum Feature Size	Tolerance	Production Rates	Materials
Micro-extrusion	Plastic deformation by force	50μm	5μm	High/mass Fair	Ductile metals
Micro-moulding/ casting	Melting and solidification by heat	25-50μm	5μm	High/mass Fair accuracy	Polymers/metals
Mechanical micro-machining	Chip formation by force	10μm	1μm	High MRR High accuracy	Metals/ polymers/ ceramics
Micro-EDM	Melting/ breakdown	10μm	1μm	High MRR High accuracy	Conductive materials
Excimer laser	Ablation by laser beam	6μm	0.1-1μm	Low MRR High accuracy	Polymers/ ceramics
Short-pulse laser	Ablation by laser beam	1μm	0.5μm	Low MRR High accuracy	Almost any
Focused ion beam	Sputtering by ion beam	100nm	10nm	Very low MRR High accuracy	Tool-steels, nonferrous, plastics

Chapter 3

Materials, Methods and Equipment

3.1 Introduction

This study examines the effects of laser processing parameters on the resultant surface texture dimensions and the interference joint bond strength. The measured effects include the increase in the insertion diameter and the surface roughness. These were processed using the parameters such as the laser power, P, focal position, z_f and scanning speed, v at different levels on the specimens. The study involved statistical analysis of the response surface models of the process parameters and error of the experiment. The work involved initial screening experiments to select the process parameter range before carrying out the full factorial design of experiments. The main laser powers applied were 300 , 400, 500 W, percentage pulse overlaps of -20, 0 and 20%, and a laser focal position 1.5 mm above, below and on the specimens. The specimens were investigate in insertion and pull-out tests.

3.2 Materials and Equipment

3.2.1 Sample Preparation

10 mm diameter pin steel samples were sectioned to 60 mm length as shown in Figure 3-1 by a Buehler Abrasimet 2 abrasive wheel cutter. The hub samples had an internal diameter of 10.05mm and an external diameter of 30mm with thickness of 10mm length of the specimens. The dimensions of the prepared interference fit parts are detailed in appendix A.2.

Figure 3-1: 60 mm steel pin insertion before the laser texturing.

The material examined was mild steel, EN3B. Table 3-1 lists the chemical composition of the as-received rods used in this experiment.

Table 3-1: Chemical composition of mild steel EN3B used for tests.

Element %									
C	Si	Mn	P	S	Cu	Ni	Cr	Mo	Fe
0.188	0.135	0.578	0.023	0.058	0.177	0.111	0.067	0.012	98.65

3.2.2 Surface Roughening of Specimens

Since most metals are highly reflective to high wavelength lasers such as CO_2 laser, the surface of the metal samples was roughened for a better absorption of the laser radiation. The chemical and physical properties listed in Table 3-2 [55, 56].

Table 3-2: Chemical properties of the sandblasting particles [43].

Chemical composition (Soda-lime glass beads)	SiO_2	Na_2O	MgO	Fe
	<75%	<15%	<5%	<1% (max. by weight)
Physical properties	Specific gravity	Bulk density	Weight	Size (Honite 13)
	2.4 to 2.6	1.5 g/ccm	25kg	106 to 212 (μm)

The surface roughening was carried out with sandblasting media from Guyson Honite-13, (see Figure 3-2). The technical specifications of the sandblasting media are further detailed in Appendix A.3.

Figure 3-2: Sandblasting media Guyson Honite-13 used for preparation of the cylindrical pin insertions.

3.2.3 Laser Surface Texturing Experiment

A CO_2 laser system, ROFIN DC-015, was used in this work. Table 3-3 lists the technical information and specifications of this system. The laser parameters examined in the study were the laser power, P, the percentage overlap ratio, OV and the focal position, z_f. Argon gas was used as an assist gas at a pressure of 0.3 MPa on the specimen. This was delivered in line with the laser beam for the protection of the laser optics and to reduce the oxidation of the molten material.

Table 3-3: CO_2 laser specification used for laser surface texturing of the mild steel [59].

Laser Medium	CO_2 gas
Wavelength	10.6 μm
Maximum Average Power	1.5 kW
Beam Diameter	32.33 mm
Focal Length	125 mm
Pulse Mode	TEM10 mode
Beam Quality	3.8

The CO_2 laser beam of 16.1 mm diameter with a TEM_{00} mode was focused with a 125mm focal length lens and a spot size of 200 μm. This value can be calculated according to the equation 2-10 for laser spot size discussed below [16, 60, 61]:

$$d_{min} = 2.44 \times [(0.125 \times 10.6 \times 10^{-6})/0.03233] \times 2 = 0.2 \times 10^{-3}\text{m} \qquad (3\text{-}1)$$

A preliminary assessment test was carried out of the process parameters and their significant values. Figure 3-3 shows the experimental set up used in experiments.

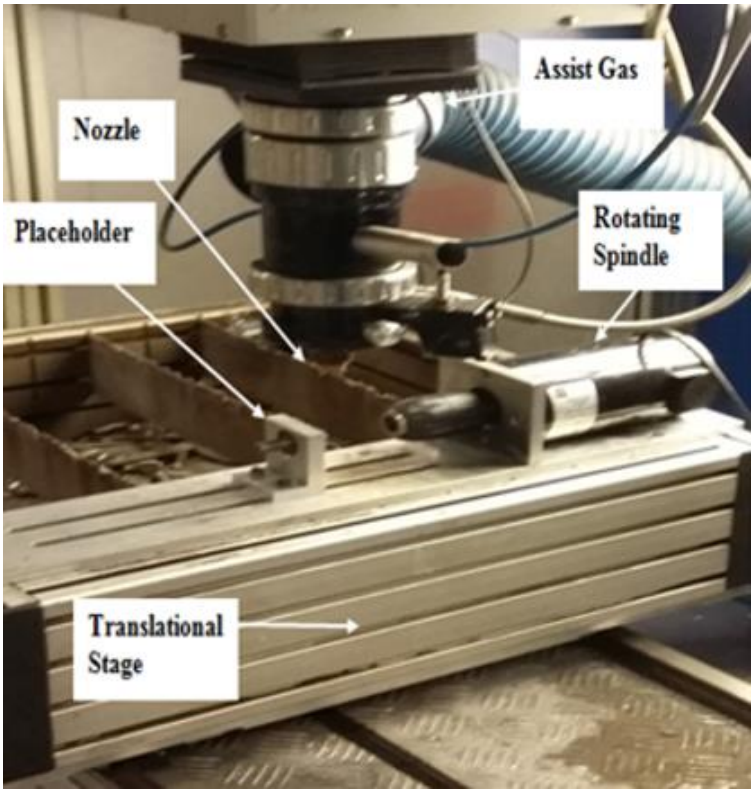

Figure 3-3: Laser system setup used for scanning of the specimen engagement length.

This CNC machine provides translation in the horizontal x and y directions. The motion of the positioning stage is controlled by the machine CNC. This provides a variable speed of 0 to 5000 mm/sec. The rotational motion of the sample was provided by means of a variable speed DC motor as shown in Figure 3-3.

3.2.4 Scanning Method Setup

The sample was placed in the variable speed DC motor spindle. The positioning stage was moved to the coordinates (0,0) below the laser. This was performed using the X, Y controls on the Rofin unit. The positioning stage was moved during process with 10 mm length on the pin in the X direction.

Laser scanning involved numerous grooves being produced on the cylindrical pin during the process. Melt pools developed had a distance, a, between the adjacent pools and laser spot size, d, that are elliptical in shape. This was observed at high scanning speeds due to the laser spot being on the surface for a finite time period of the process. This is as the sample moves beneath the laser.

Figure 3-4 gives the position of the various parameters. This describes the design of scanning pattern of the grooves on the workpiece.

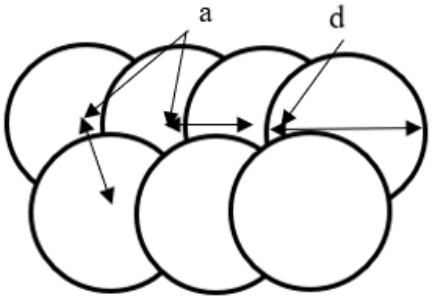

Figure 3-4: Schematic of the dimensions of the laser spot scanning on the samples.

The laser scanning speed determines the distance, a, of surface textures. These layers overlap each other and the width, d, of the surface textures on the processed material.

3.2.5 Preliminary Test

The test involved screening the parameters using visual observation for increase of diameter, consistency of surface textures and reduction of oxidation of the samples. The parameters examined were the laser power, the focal position, the percentage of the overlapped laser pulses, the assist gas pressure and the pulse repetition frequency. The

process parameters were always set to be slightly above the melting point in order to avoid any over-melting, oxidation and the loss of the material. These three parameters at three set levels were selected for experimental work, i.e. the laser power, the percentage overlap and the focal position. A response surface method of 27 experiments using 3 factors and 3 levels for full factorial design of experiment model was implemented for the experimental work. Figure 3-5 shows the setup of the laser processing of cylindrical samples and the direction of the overlap of the surface textures on the samples.

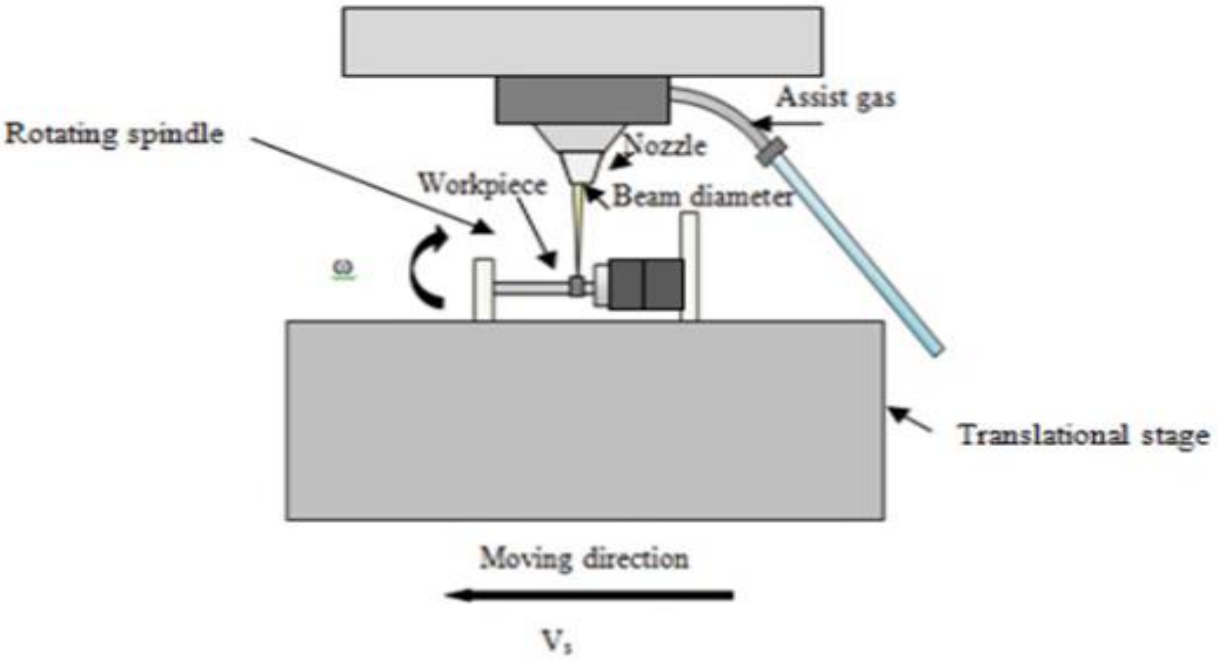

Figure 3-5: Schematic of the laser processing method of the cylindrical samples.

3.2.6 Design of Experiments

The parameters and their levels were prepared in Design of Experiments (DoE) using response surface methodology design. This was used for optimising of the laser power, focal position and percentage pulse overlap. The study involved a full factorial analysis of specimens with n factors and k levels of the parameters. The design of experiments consisted of experiments using factorial experiment of the parameters. Therefore, for analysis of laser power, focal position and percentage overlap, there were 27 runs. The investigation was used to study the effects and interactions of the parameters on the responses. The parameters were used to develop a method process map of the optimum levels.

Table 3-4 shows the control panel settings used for laser surface texturing of the cylindrical pins. The responses measured were the diameter increase, surface roughness and average insertion and pull-out force of the samples. Table 3-5 list the nominal values of the parameters is summary form.

Table 3-4: Process parameters and control panel settings used for the laser surface texturing of the specimens.

Sample No.	P (W)	z_f (mm)	O.V (%)	Duty Cycle (%)	τ (ms)	PRF (Hz)
1	500	-1.5	-20	50	8.06	100
2	500	0	20	50	12.00	100
3	400	1.5	20	50	12.10	100
4	500	0	0	50	10.00	100
5	300	0	0	50	10.00	100
6	500	1.5	0	50	10.08	100
7	400	-1.5	-20	50	8.06	100
8	300	0	-20	50	8.00	100
9	400	-1.5	0	50	10.08	100
10	400	1.5	0	50	10.08	100
11	300	-1.5	0	50	10.08	100
12	300	1.5	-20	50	8.06	100
13	500	1.5	-20	50	8.06	100
14	500	1.5	20	50	12.10	100
15	400	0	20	50	12.00	100
16	400	0	0	50	10.00	100
17	400	1.5	-20	50	8.06	100
18	500	-1.5	20	50	12.10	100
19	400	0	-20	50	8.00	100
20	300	-1.5	-20	50	8.06	100
21	300	0	20	50	12.00	100
22	500	-1.5	0	50	10.08	100
23	400	-1.5	20	50	12.10	100
24	300	1.5	20	50	12.10	100
25	300	1.5	0	50	10.08	100
26	300	-1.5	20	50	12.10	100
27	500	0	-20	50	8.00	100

The factorial design enables a polynomial equation to be generated relating the input process parameters to the resulting outputs of the experiments. A cubic model was suggested for surface responses in the fit summary as adequate to determine the effects and interactions of the parameters. The response surface method was used for optimising the process parameters. This involved using 3 input variables (factors) to measure the response from experiments. The statistical significance of laser parameters was also be calculated from the Design of Experiments.

Table 3-5: Factors settings for the Response Surface Model.

Factor	Process parameter	Units	Lower Level	Mid-Level	Higher Level
A	Power	W	300	400	500
B	F. P	mm	-1.5	0	1.5
C	O. V	%	-20	0	20

3.3 Measurement of Diameter Increase and Average Roughness Parameter

The diameter increase measurements were taken with a Vernier calliper at 3 intervals across the laser surface textured samples. These were averaged to give the result. The measurement instrument had a resolution of 0.05 mm. The surface roughness was determined using the equation for a CNC milling machine with a rotation speed, N and a translation speed, v_f of a rotating spindle in equation 3-8.

3.4 Surface Topography Measurements

3.4.1 Chemical Etching

Specimens were prepared and cleaned with ethanol before microscope measurements of the surface. The chemical etchant was composed of 1-5ml HNO_3, this was used to prepare nital solution of 5% by volume solution for the specimens. This was poured into the ethanal solution until there were gas evolution, this surface preparation consisted of nital solution etch of 5% HNO_3 for 10 minutes on the sample, details are shown in Table 3-6.

Table 3-6: Etchants used for surface treatment of the specimens for the microscope measurements [33].

Etchant	Composition	Volume	Use
Nitric acid (nital)	HNO_3 Ethyl or Methyl alcohol	1-5 ml 100 ml	Etching rate increased or selectively decreased with amount of HNO_3. SWAB for a few second to 1 min. In carbon steels: (1) to darken pearlite and give contrast between pearlite colonies; (2) to reveal ferrite boundaries; (3) to differentiate ferrite from martensite

Chemical etching removes layers of grain boundaries and structures from the surface of the samples. The surface condition before observing under the microscope is an important factor for analysis of the specimens. This can used to clearly observe the phase structures.

3.4.2 Microscope Measurements

The Keyence VHX 2000E 3D microscope was used to take images of the samples. These were used to analyse the microstructure of the surface of the specimens. The equipment has a resolution of 0.1μm. The samples were placed on the XY stage of the microscope. This had a high-performance objective for images at 100μm resolution with a large depth of microstructure of the parts. The microscope objective was positioned at 90º angle to the surface. The measurement of the surface roughness parameters and the morphology were then processed with image processing software ImageJ. This microscope was used for analysis of the characteristics of surface roughness of the samples is shown in Figure 3-6.

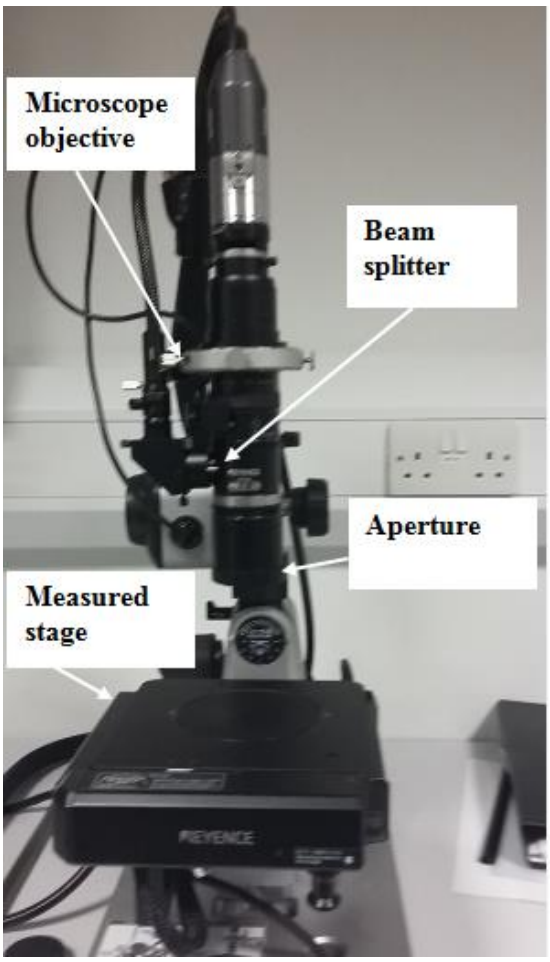

Figure 3-6: Schematic of the Keyence VHX 2000E microscope used for measurement surface topography of samples.

3.4.3 Measurement of Texture Angles, Peak to Peak Widths, Peak to Valley Depths Parameters

The surface profile affected the strength of the fabricated interference fit joints. The parameters produced profiles of different dimensions on all of the 27 samples. The microscope observed effects of the process parameters on the surface topography of the specimens. Figure 3-7 shows the schematic highlighting the measurements taken of the surface topography of the specimens. This was using the ImageJ software for image processing of the specimens.

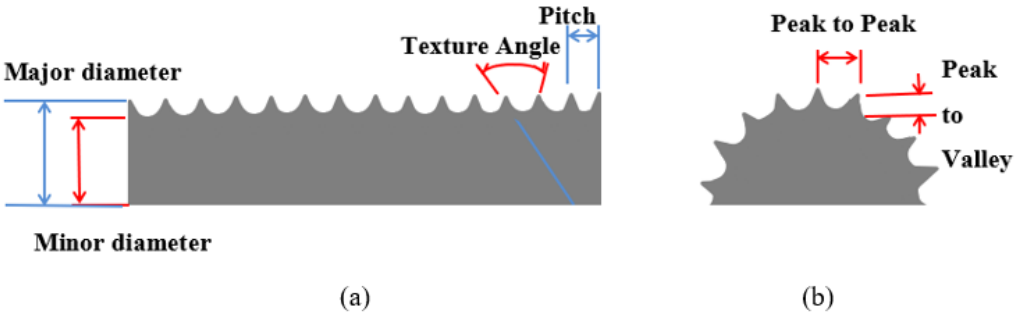

Figure 3-7: Schematic of (a) dimensions, texture angle and pitch and (b) peak to peak widths and peak to valley depths of the interference fit pin.

3.5 Insertion and Pull-Out Test

The insertion and pull-out tests were carried out on Zwick Z-50 testing machine The test was performed with the Zwick TestXpert simulation software for insertion and pull-out forces of the samples. Figure 3-8 shows testing machine programmed to apply an insertion load at a rate of 5mm/min on the pin specimens. This resulted in deformation of the specimens. The insertion and pull-out test resulted in low strain rates according noted standards in the Appendix C.1.

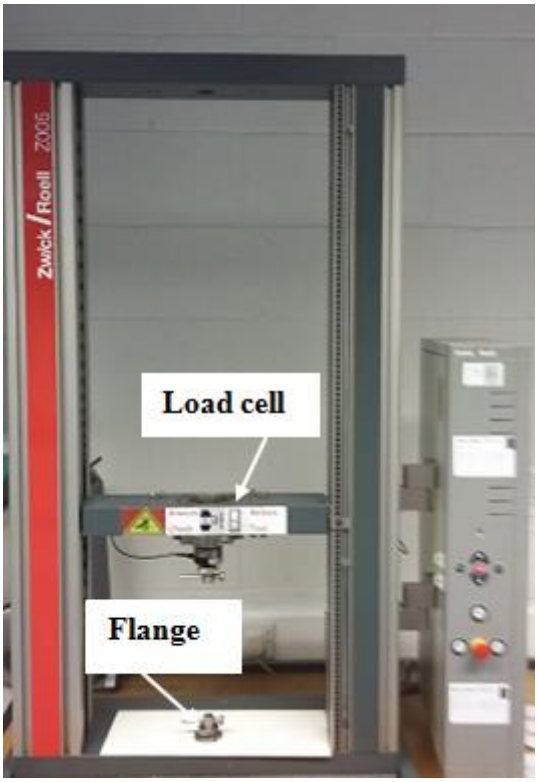

Figure 3-8: Schematic of the Zwick Z-05 testing machine used to measure the insertion and pull-out forces of the specimens.

Chapter 4 Results

4.1 The increase in diameter

From visual observation, the sample diameter significantly increased with the levels of the process parameters. The experiments resulted in a diameter increase ranging between 10.2mm to 10.8mm.

The following equation was obtained by the DoE model correlation of the input processing parameters. This was applied for the range of increase in the sample diameter as an output. This equation of diameter increase can be used to predict the effects of the parameters but not with a high level of precision of the results. This was determined with an insignificant p value of 0.0626, adjusted R-squared of 0.3698 and Predicted R-squared value of -0.0472 and does not have agreement. The deviation that can be found in this equation from the experimental results could be explained by the interpolations used in the DoE software and the interpolation applied when calculation the processing parameters. The stochastic nature of the process is highlighted here in that not every model can predict the output of this process. Further experimental points and results could be used to increase a DoE predictive accuracy, see discussion in Chapter 5.

Diameter increase = 15.9284 + -0.0180556 * Power + -1.82469 * F.P + -0.0319444 * OV + 0.0027963 * Power * F.P + 0.000127778 * Power * OV + 0.00361111 * F.P * OV + 3.53704e-005 * $Power^2$ + -0.832922 * $F.P^2$ + 0.00199537 * OV^2

Table 4-1 lists the measurements of average increase in the insertion diameters, D_{avg} and the standard deviation, σ_{avg} of the 27 samples. The results show that the settings of laser power P, focal position z_f, and the percentage overlap O.V correlation on the increase in the pin diameter. The focal position and the percentage overlap were the most significant on the response of the diameter increase of the samples. The model of the diameter increase shows a strong fit with the measured response of the samples. This shows that each parameter had a significant effect on the surface response of the diameter increase of the specimens.

Table 4-1: Measured insertion diameter and predicted values as a function of the process parameters.

Sample No.	P (W)	z_f (mm)	O.V (%)	D_{actual} (mm)	D_{pred} (mm)	Error (mm)
1	500	-1.5	-20	10.7	14.8	4.1
2	500	0	20	10.7	17.2	6.4
3	400	1.5	20	10.2	12.7	2.6
4	500	0	0	10.8	15.7	4.9
5	300	0	0	10.4	13.7	3.2
6	500	1.5	0	10.3	13.2	2.9
7	400	-1.5	-20	10.5	14.1	3.6
8	300	0	-20	10.4	14.4	3.9
9	400	-1.5	0	10.3	13.6	3.3
10	400	1.5	0	10.4	11.4	1.0
11	300	-1.5	0	10.3	13.3	3.0
12	300	1.5	-20	10.1	10.9	0.8
13	500	1.5	-20	10.2	13.3	3.1
14	500	1.5	20	10.5	14.8	4.3
15	400	0	20	10.4	15.5	5.1
16	400	0	0	10.3	14.4	4.0
17	400	1.5	-20	10.1	11.7	1.6
18	500	-1.5	20	10.7	15.8	5.1
19	400	0	-20	10.5	14.8	4.3
20	300	-1.5	-20	10.3	14.1	3.8
21	300	0	20	10.4	14.6	4.2
22	500	-1.5	0	7.0	14.5	7.5
23	400	-1.5	20	10.5	14.6	4.1
24	300	1.5	20	10.1	11.4	1.3
25	300	1.5	0	10.0	10.3	0.3
26	300	-1.5	20	10.5	14.1	3.6
27	500	0	-20	10.5	15.9	5.4

Figure 4-1 shows the response surface plots for the effect of the power, focal position and overlap ratio on the increase of diameter. A clear correlation between the increase in diameter and lowering the laser beam focal position was observed for the specimens. This was due to the increase in the thermal energy applied and the larger observed resultant melt pool.

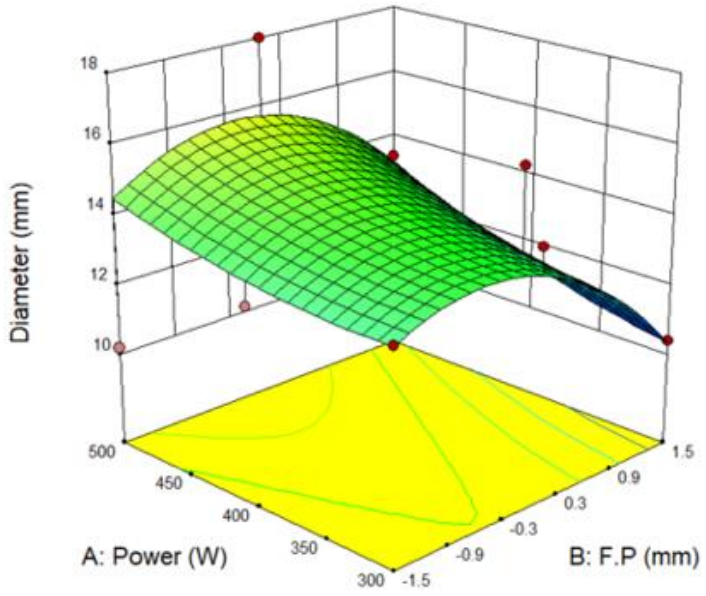

(a)

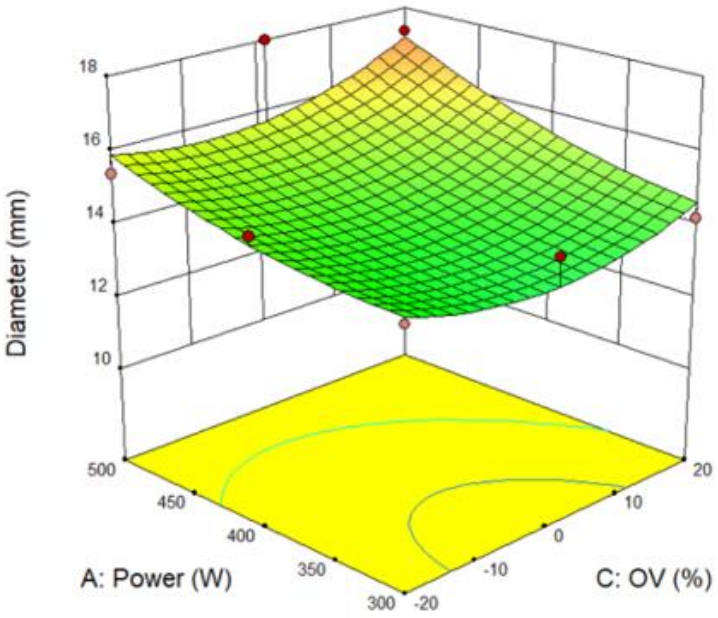

(b)

Figure 4-1: Effects process parameters on diameter for (a) laser power and focal position and (b) laser power and percentage overlap.

4.2 Measurements of the Surface Roughness

The surface roughness was calculated by using the method explained in section 2.7. The measured surface roughness exhibited a clear correlation with the input process parameters for all different levels. The DoE model shows a significant analysis represented by the p-value of 0.05. The following mathematical equation of the model of surface roughness to predict the effects of process parameters. The model shows a p value of 0.0857 is significant in for analysis of the process parameters. The results also have an adjusted R-squared of 0.8769 and predicted R-squared value of 0.7898 agreement. This model predicted that the results of the process parameters effects on the experiment with precision.

Surface Roughness = 58.0473 + -0.0351683 * Power + 8.47419 * F.P + -1.15767 * OV + -0.0143501 * Power * F.P + 0.000379863 * Power * OV + -0.101202 * F.P * OV + $6.5876e^{-006}$ * $Power^2$ + 3.29185 * $F.P^2$ + -0.00164707 * OV^2

Figure 4-2 shows the response surface plot of the surface roughness of the processed samples. The graph shows that the surface roughness decreases as the laser beam focal position is near the sample surface. Moreover, a clear reduction in the surface roughness was observed with the increase of the scanning tracks overlap. This result can be explained by the re-melting of portion of material from the previous scan track on the specimens. These laser scanning grooves interfere with the current track rather than leaving un-processed gaps in the case of the negative overlapping scanning scenarios. The zero focal position scenario (focus on the surface) means the application of the maximum thermal energy density on the specimen. This produces less amount of pores on the surface.

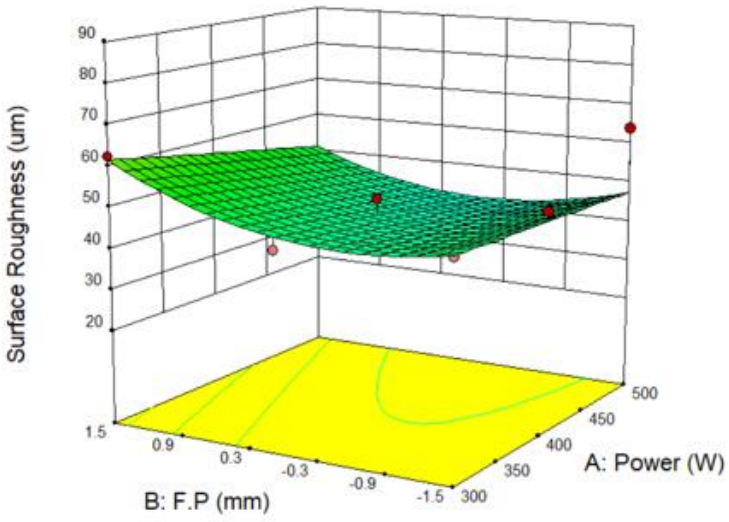

(a)

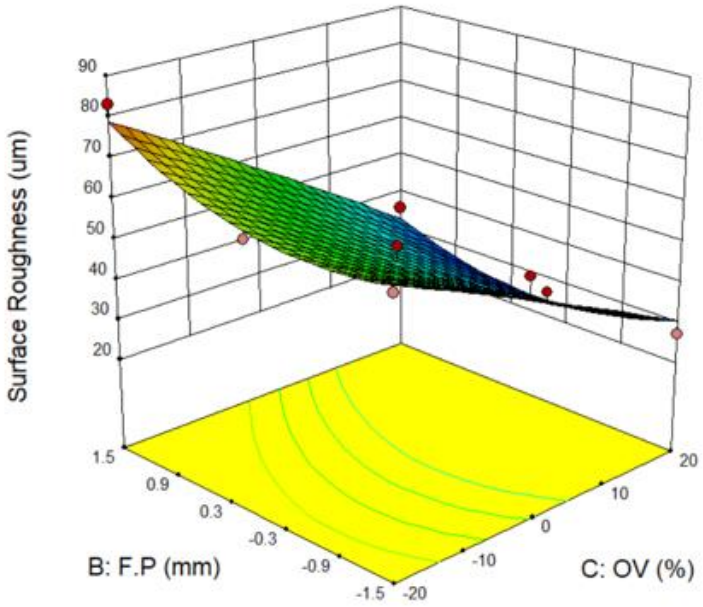

(b)

Figure 4-2: Effects of the process parameters on surface roughness for (a) percentage overlap and focal position and (b) percentage overlap and laser power.

4.3 Effects of Measurement of Texture Angles, Peak to Peak Widths and Peak to Valleys Depths

Table 4-2 lists the texture characteristics for six samples. This shows the maximum and minimum forces during the assembly and disassembly test.

Table 4-2: Surface texture dimensions from insertion and removal tests of pin into the hub joint.

Sample No.	Peak to Peak Widths, RSm (μm)	Peak to Valley Depths, Rq (μm)	Texture Angle, θp (degrees)	Aspect Ratio, S/R	Profile Type
1	241 ± 10.1	431 ± 49.1	60.0	1.79	Ridged
3	269 ± 6.68	473 ± 0.5	61.6	1.76	Ridged
9	253 ± 16.8	473 ± 67.8	61.8	1.87	Ridged
15	241 ± 3.98	435 ± 5.2	61.6	1.81	Textured
21	228 ± 4.45	413 ± 17.4	61.0	1.81	Ridged
23	259 ± 16.5	451 ± 47.6	29.3	1.74	Ridged

The investigated showed two types of texture, the Ridged texture in which a clear texture angle and the Textured where there is no texture line on the specimens.

Figure 4-3 shows the two types of surface profiles from experiments of the laser processing parameters.

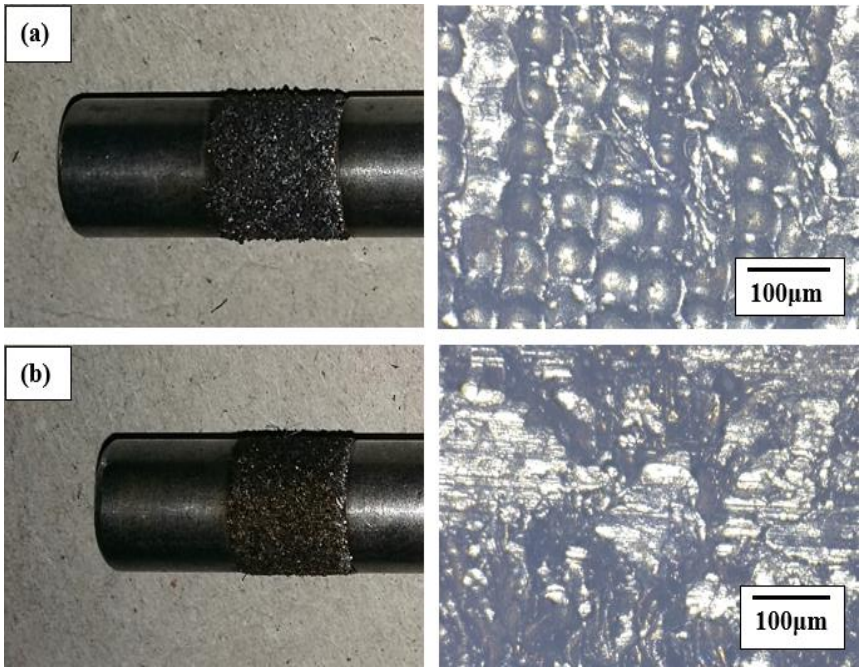

Figure 4-3: Specimens shows sample (a)15 at 400W and (b) 21 at 300W and constant percentage overlap and focal position

Based on the images gained from the optical microscope, the surface topography on the macroscopic level for both samples no. 15 and 21 are similar. Similar focal position and percentage overlap was used with laser beam power of 400 and 300 W respectively. This process resulted in transition of morphology from dimple-type textures to ridged surface topography

Figure 4-4 shows the average peak to valley depths of the surface texture for the 27 samples. This indicates a small variation in the measured values except for samples no. 24 and 25 where negligible diameter increase of 10 and 10.1mm in the texture height was produced.

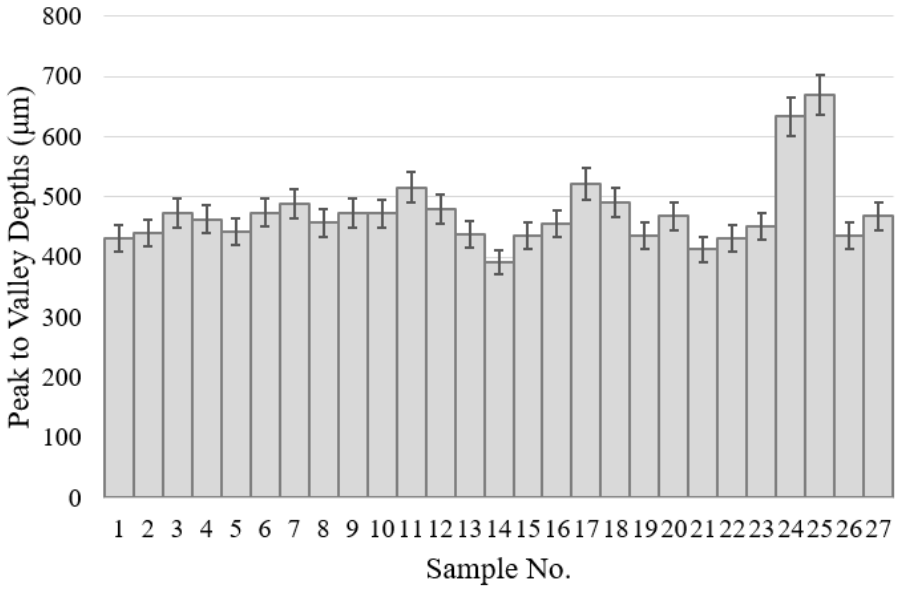

Figure 4-4: Graph of the average peak to valley depths of surface texture of the specimens.

Figure 4-5 shows the peak to peak widths for the 27 samples. The figure indicates a limited variation in the measured values.

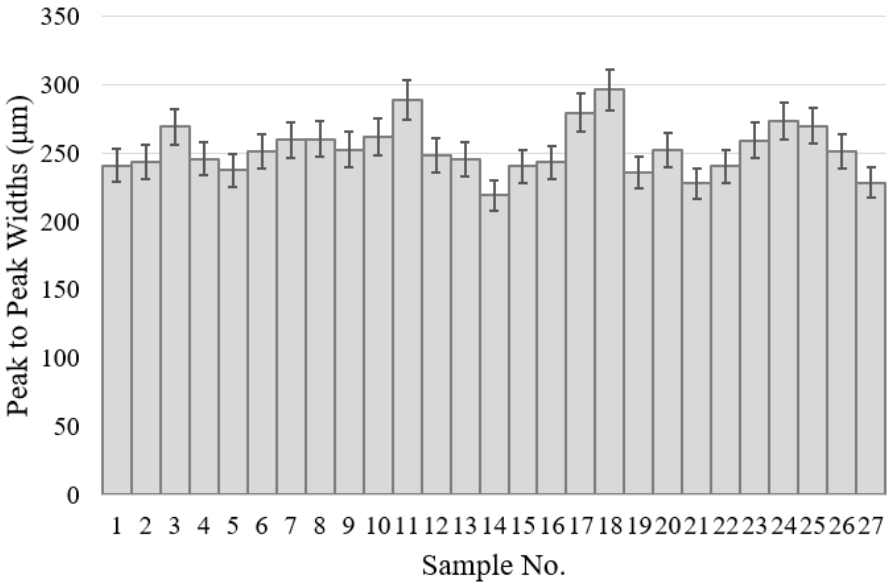

Figure 4-5: Graph of the average peak to peak widths of the surface textures of the specimens.

4.4 Insertion Force and Pull-out Test Results

The test result were divided according to the highest, average and lowest insertion and pull-out forces. This was to investigate the material's ability for resistance to deformations and failure of the joint. The insertion and pull-out force correlation was calculated using the correlation coefficient R^2 of the regression line for spatial parameters. Figure 4-6 shows a 3D plot of the effect of the laser beam power and focal position on the resultant insertion force for a 0% overlap.

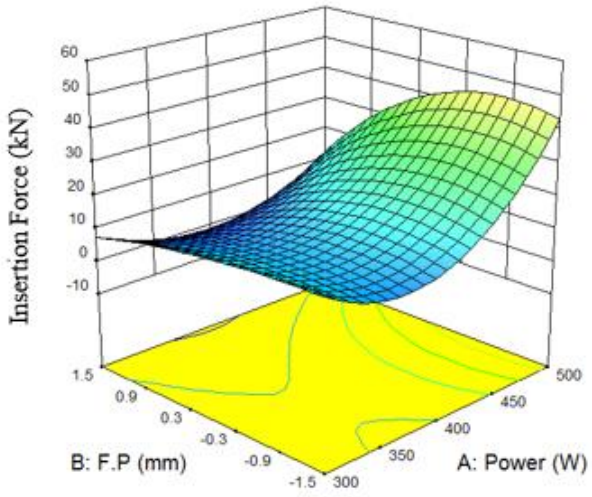

Figure 4-6: Effects laser power and focal position processing parameters and the insertion force.

4.4.1 Lowest strength insertion

Figure 4-7 and 4-8 show the plot of insertion and pull-out forces. These define of strain in the material. The samples exhibited a continuous and significant grip between the mating parts during the removal test. Compared to the traditional press-fit joint which suffer from sudden failure, this performance provides safer working conditions for the specimens. This gave a pre-notice of the joint failure to the operator. This was to stop the machine and replace the joint.

Figure 4-7 shows the insertion force of the lowest strength samples from experiments of the pin and hub joint.

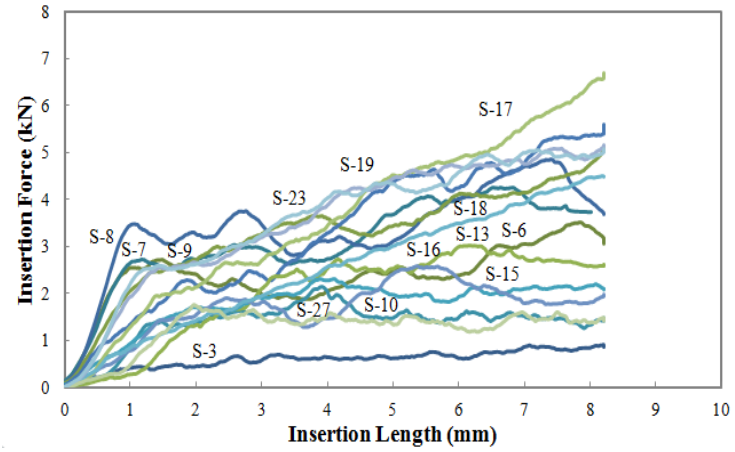

Figure 4-7: Graph showing the range of insertion values of the lowest strength samples.

Figure 4-8 shows the pull-out forces of the samples that had the lowest strength upon removal of the pin from the hub joint.

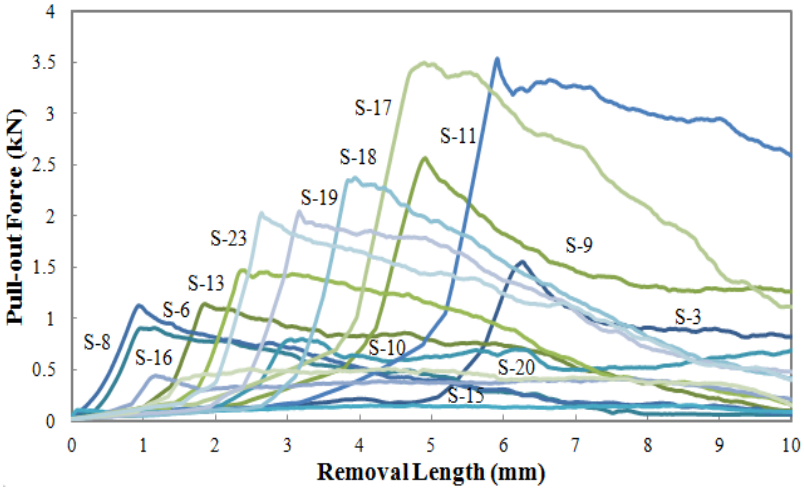

Figure 4-8: Graph of the range of pull-out forces of the lowest strength samples.

These test results were obtained with a diameter increase of 10.3 ± 0.1 mm. Figure 4-9 shows the lowest strength specimens which had the average of the insertion and pull-out forces of the range of specimens. This resulted in an error bar of 95% confidence interval of the insertion response of the pin and hub joint.

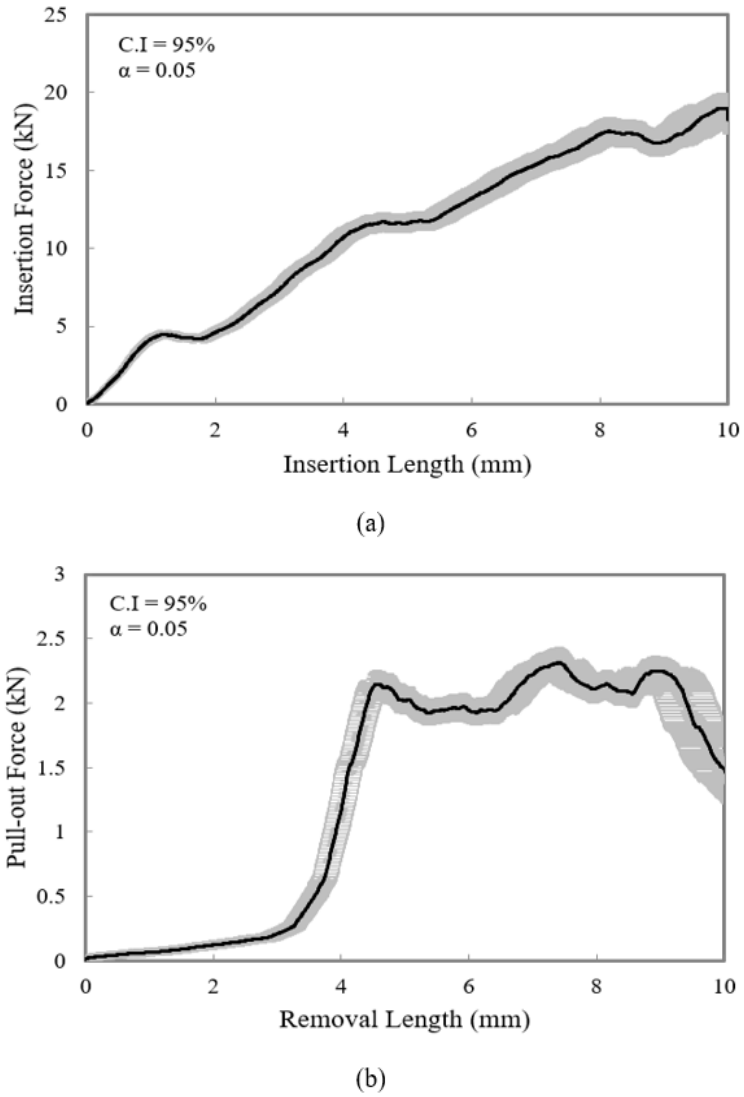

Figure 4-9: Graph of insertion and pull-out forces of (a) samples 2 at intermediate strength and (b) samples 14 at lowest strength test.

The test results obtained an average surface roughness of $14.02 \pm 8.29 \mu m$ due to high plastic strains of specimens. The samples shows of the analysis is reproducible effects of the process parameters on the surface roughness.

4.4.2 Intermediate strength insertion

Figure 4-10 and 4-11 show the insertion and pullout test results of the samples that show significant plastic deformation with relatively higher bond strength than that in the previous section.

Figure 4-10 shows the insertion test results of the sample that had intermediate strength between the pin and the hub joint.

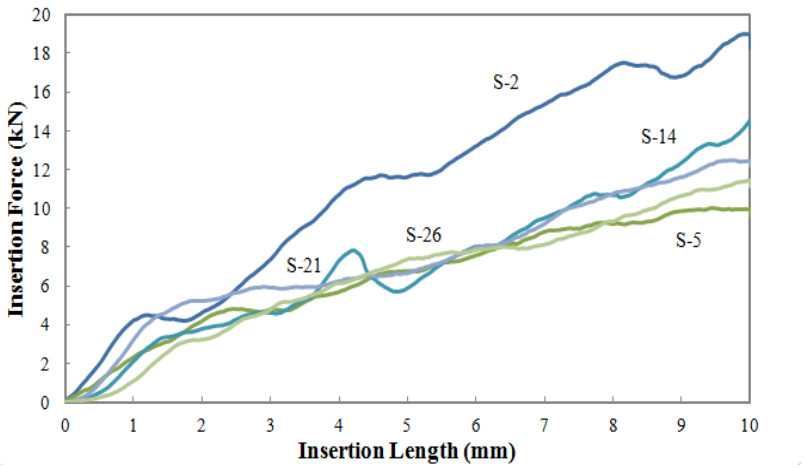

Figure 4-10: Insertion force measured over insertion length of the intermediate strength samples.

Figure 4-11 shows the pull-out test results of samples that had intermediate bond strength during the removal of the pin from the hub joint.

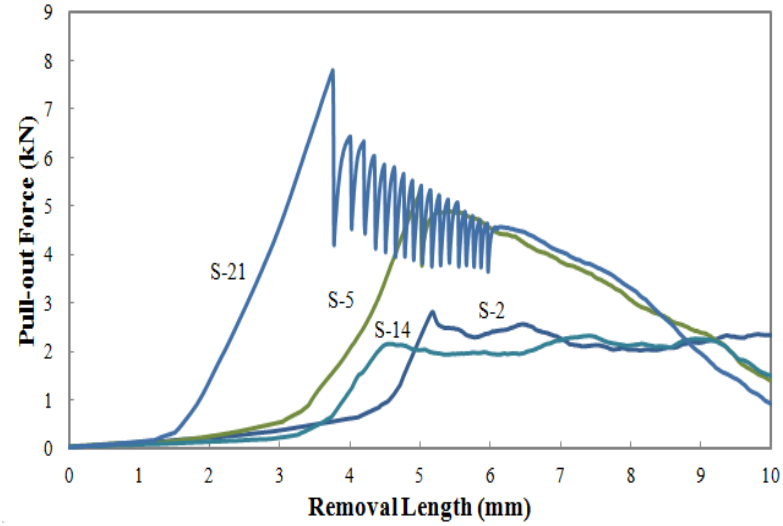

Figure 4-11: Pull-out force measured over removal length of the intermediate strength samples.

The pull-out test results showed a diameter increase of 10.5 ± 0.1mm. This obtained a correlation on the increase of diameter of specimens. The following Figure 4-12 shows the specimens which had average insertion and pull-out forces with the 95% error bar confidence interval.

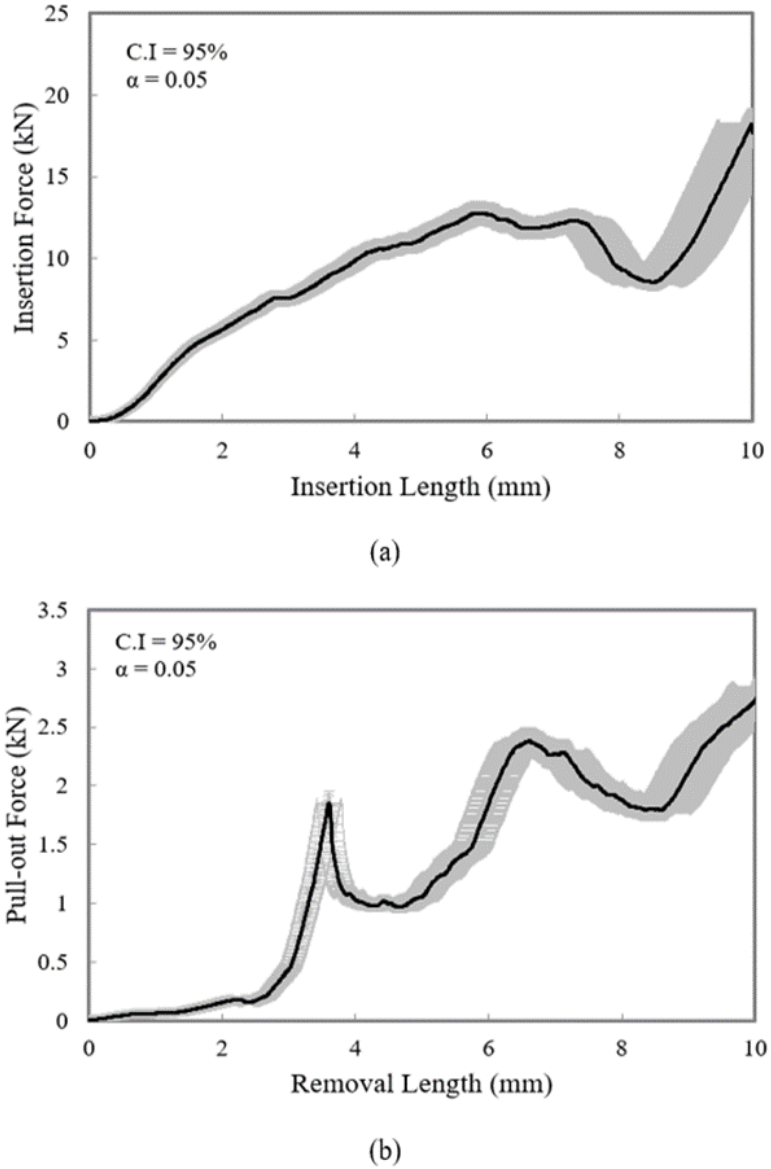

Figure 4-12: Graph of insertion and pull-out forces of (a) sample 27 and (b) sample 24 that that were the intermediate strength specimens using test.

4.4.3 Highest strength insertion

Figure 4-13 and 4-14 shows the insertion and pull-out test results of the samples. These samples had the highest insertion and removal forces. The samples show low strain rates but high insertion forces due to tests of the specimens.

Figure 4-13 shows the insertion test results of samples that exhibited the highest strength of insertion of all the samples.

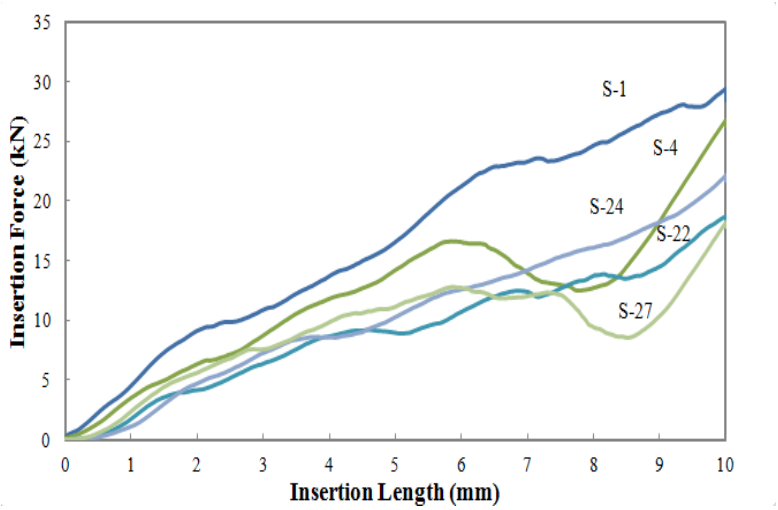

Figure 4-13: Insertion force over the insertion length that had the highest strength samples.

Figure 4-14 shows the samples that obtained the highest bond strength during removal of the pin from the hub joint.

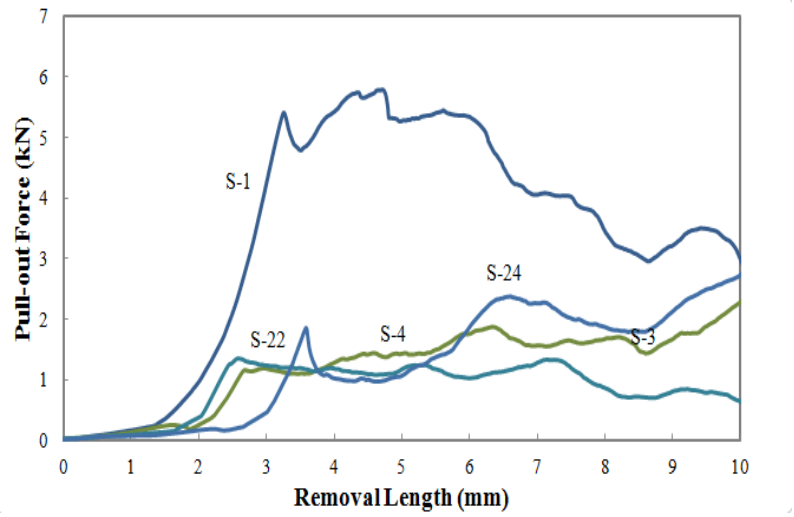

Figure 4-14: Pull out force over the removal length that had the highest strength samples.

The insertion test results obtained average diameter increase of 10.5 ± 0.033mm. Figure 4-15 shows the highest strength specimen. These samples were measured an average of the

insertion and pull-out forces of range of specimens. This resulted in an error bar used of 95% confidence interval of the responses of the pin and hub joint.

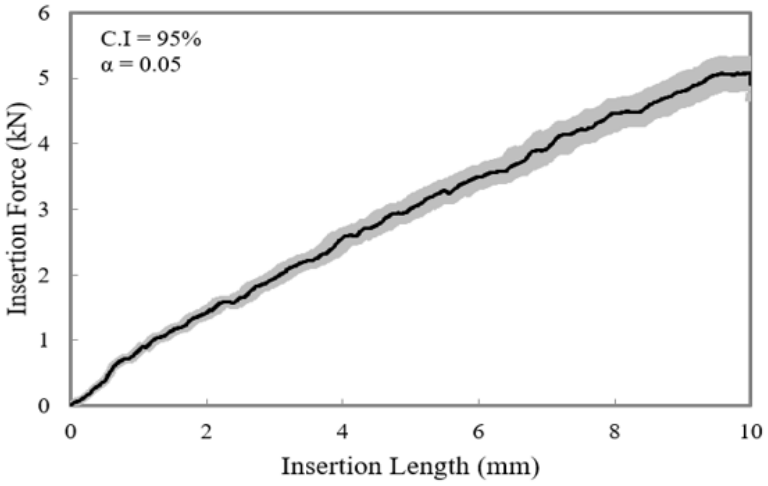

(a)

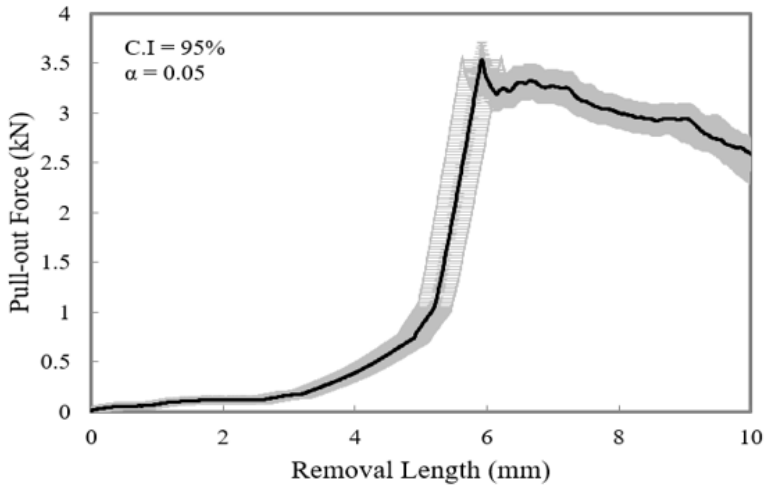

(b)

Figure 4-15: Graph of the insertion and pull-out forces of (a) sample 18 and (b) sample 11 that were highest strength samples using test.

The ranges of insertion and pull-out test results obtained an average surface roughness of $13.2 \pm 14.6\mu m$ from the specimens.

Chapter 5 Discussion and Conclusion

5.1 Analysis of Process Parameters on Diameter Increase

In this study, a CO_2 laser beam was employed in the pulse wave operating mode. Laser beam in the pulse operating mode was used to melt a controlled layer thickness from the steel sample surface. This involved the rotational movement, the resulting centrifugal force and the overlapping scanning tracks of the molten material. The laser scanning is relocated and created a controlled and predicted surface texture increase in the cylindrical sample diameter. This diameter increase utilises the interference press-fit assembly. The laser beam power, P, range applied was 300 to 500 W. Two other parameters were also used. Those are, the laser beam focal position, F.P, and the percentage overlapping, O.V of the laser scanning tracks. The latter processing parameter was applied in both the peripheral and longitudinal directions with the same value. Figure 5-1 shows the correlation coefficient, r of the relation between the three processing paraeters and output resulting response. This represented by the increase in the insertion diameter.

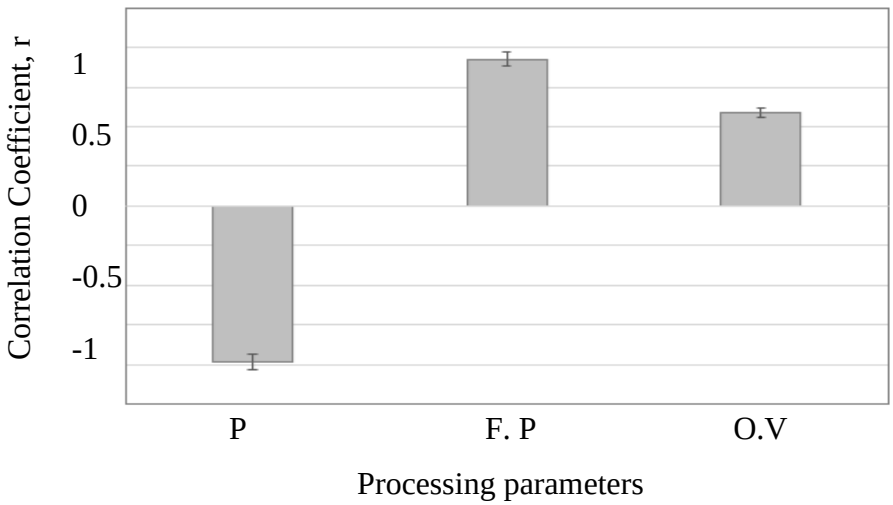

Figure 5-1: Correlation coefficient of the input processing parameters and the resulting diameter increase.

It can be observed that each of the parameters have a significant effect on the diameter increase of the specimen. The process parameters such as the laser power and focal position

were the most significant factors effecting the response. From the results table, it can be concluded that the optimal configuration was the laser power of 500W, focal position of 1.5mm below the surface and percentage overlap of 20% of the spot on the specimen. This resulted in a maximum diameter increase of 10.8mm. Moreover, Figure 5-1 indicates that all the processing parameters have a strong correlation with the increase in the insertion diameter for the working range level. The laser power showed a 0.54 correlation on the increase of diameter of the specimens. This can be explained by the over-melting and the large melt pool size generated at the high levels of 500 W. In this case, some of the molten material is prone to be ejected and removed due to the centrifugal force and the gas ejection on the specimen. This resulted in a reduction in the texture height. Both the focal position and the percentage overlap show a direct proportional correlation with the diameter increase. This can be explained by the build-up of the new material coming from the current scanning track from the previous one. It is also clear from this Figure 5-1 that the processing parameters levels showed strong correlation with the diameter increase.

5.2 Analysis of Process Parameters on the Surface Roughness of the Samples

Figure 5-2 shows that the percentage overlap has a strong correlation with the surface roughness of the samples. The other two processing parameter showed less strength correlation at the working level of these parameters.

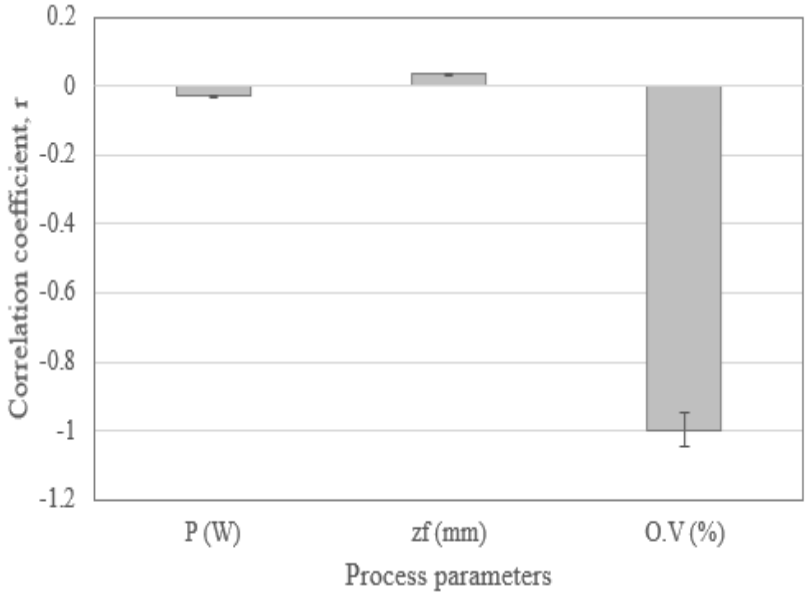

Figure 5-2: The correlation coefficient of the input processing parameters and the surface roughness measured.

These were close to each other enough not for a wide variation in the surface roughness. This shouldn't be a problem because the focus in this study was to achieve the higher diameter increase. The processed samples showed that the maximum diameter increase at 20% overlap. As explained earlier, this was due to the build of the molten material in the current scan track on the specimen. The previous track and the fact that they are rigidly (mechanically and chemically) bonded on the specimen. This is by re-melting 20% of the solid material. From Figure 5-2, the overlapping scanning tracks exhibited an inverse correlation with the resultant surface roughness of the textured surface. This means that the un-processed gaps between the consecutive tracks resulted in a deep valleys and waving of surface textures. This observed compared to the raised texture peaks. The resultant surface roughness range obtained in this experiment was from 28 to 87 microns.

5.3 Laser Processing Regime

The surface modification had a range of conditions from heating to significant melting of the Mild Steel EN3B using the CO_2 laser. The melt pool for three characteristic samples and process parameter levels are displayed below:

Figure 5-3: Laser processing regimes for three different samples processed at (a) 1.85 MJ/mm^2 (b) 2.23 MJ/mm^2 and (c) 0.186 MJ/mm^2 laser energy densities.

Figure 5.3 (a) shows sample 24 had dimple surface textures uniform distribution across the specimens. Figure 5.3 (b) shows sample 11 has the onset of the development of columnar grains in the melt pools. Figure 5.3 (c) shows sample 27 has a considerably large grain structure due to the higher laser absorption on the specimen. Thus increasing the depth of the melted material in comparison to the other samples with higher laser energy densities on the specimen. Samples 24 and 11 showed a lower deviation of the depth of the melt pool due to the lower variability in the geometry of the melt pool on the materials.

As can be observed for the samples there are three different regimes of laser interactions that include heating, melting and significant melting of the pin specimens. The laser beam absorption of the bulk material by the three specimens was mainly the cause as it acts as the medium for heat transfer from the surface. The laser overlap percentage and focal position had a significant contribution to these laser processing mechanisms. Figure 2 (a) was processed at 20% percentage overlap and a hatch spacing of 0.161mm. This gave it a lower depth of processing and high laser energy density and a hardened depth during the laser heating regime. Figure 5.3 (b) was developed at 0% percentage overlap and spacing distance of 0.2mm. This resulted in a lower grain depth and melt pool with some changes to the structure of the bulk material. Figure 5.3 (c) was laser scanned at -20% overlap for a distance between scanning tracks of 0.24mm on the pin specimen. This was in the laser melting regime as the previous sample. Due to the extensive depth and laser absorption produced much higher residual streses and crack formation by the surface and the surrounding bulk material. As can be observed there is considerable redistribution of the surface for the formation of the melt pool. The laser energy density resulted in wear of the surface without any mass loss due to evaporation of the pin specimen.

5.4 Phase transfer and the oxide layer

The microstructure exhibited an oxide layer which are hard metal grains on the surface (shown in the Figure 5-4) due to the high cooling rate during the laser melting and re-solidification. The main role of the assist gas was to mitigate the oxidation effect on the specimen. This was to protect the laser optics from any raising fumes. The oxide layer formations is not avoidable because the process is carried out in an open environment and the assist gas is diluted by air. The thickness of the oxide layer depends on the laser power level and the scanning speed in which the laser-material interaction time (residence time) is related. The higher the oxide layer thickness the more brittle the surface texture and the easier to break during the insertion process.

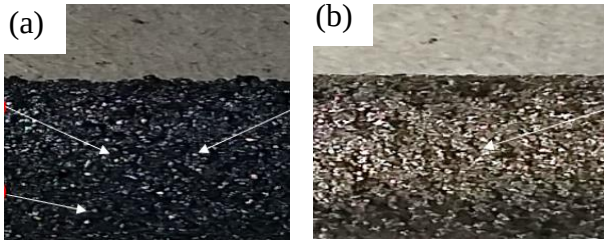

Figure 5-4: (a) Sample no. 2 processed with 500 W, and 20% OV, and (b) Sample no. 12 processed with 300 W and -20% OV.

The samples which exposed to high power level and long exposure time exhibit more oxide on the surface with the fracture of most of the textured material during the insertion process. As a result, no sufficient amount of material remain in the interface area and low clamping force is presented and thus the joint is easy to break. The following Figure 5-3 shows a comparison between sample no. 2 and sample no. 12. Sample no. 2 processed with the higher amount of thermal energy produced by 500 W, laser spot positioned on the sample surface and 20% OV. The darker colour compared to that of sample no. 12 which is processed with 300 W, 1.5 mm above the surface and -20% overlap, is an indication of the brittle oxide layer.

5.5 Insertion and Pull-out test

Based on the removal test and the pull-out performance of the joint assembly. It can be seen in Figures 4-8, 4-11 and 4-14, that the failure of these insertions is safe compared to the traditional press-fit joint which in most cases suffer from sudden failure. There is continuous gripping of the pin inside the hub after the first failure point of the specimen. This offers a pre-notification to the operator. To stop the machine and replace the assembly.

The insertion and pull-out forces studied using statistical analysis of each joint assembly. The test results show a strong correlation with the input processing parameters. This produced a range of insertion forces of 0.931kN to 29.4kN and pull-out forces of 0.15kN to 7.8kN.

5.5.1 Insertion and Pull-out Test for the Laser processing Regimes

Removal test until failure of the surface textures produced friction in some specimens and led to flank wear in other specimens. The surface textures of the three different regimes had different friction coefficients between the contact surfaces given in Figure 5-5.

Figure 5-5: Pull-out test results of the pins for (a) sample 24, (b) sample 11 and (c) sample 27 in the three different laser processing regimes.

Figure 5-5 (a) shows that a translational speed of 5.1mm/min resulted in a smoother finish and hence no contact area in contact during removal tests. Figure 5-5 (b) shows at 7.6mm/min that due to the columnar geometry of the contact surface there was some contact area between the mating parts. This resulted in strain of the surface of the specimen. Figure 5-5 (c) shows that at 11.5mm/min due to the intergranular contact area there was significant wear of the surface that in the other specimen. This specimen had a lower oxidation residence due to the higher translational speed of the spot on the pin. This did not give enough assist gas flow to the specimen. Therefore, giving it the lowest oxygen percentage in the specimen.

The experiments were obtained an average joint force range of 20.2kN, 18kN and 31.2kN of samples 24, 11 and 27 respectively. This shows that sample 27 laser processing regime had the highest joint force. Thereby giving more flank wear than the other samples but sample 11 gave a considerably high joint force without high friction coefficient on the contact surfaces. This sample maintained the joint and surface quality during the insertion and removal test. Samples with this microstructure are more wear resistance with a sufficiently high load carrying capacity during assembly and disassembly of the pin from the hub joint.

5.6 Conclusion

In this study, a novel method for an interference fit joint was developed for automotive parts. The process is highly repeatable and predictable control and adjustment on the input processing parameters and the related output measured. CO_2 laser beam was used during the process due to the wide application of the laser in both academia and industry. To the authors knowledge, the process can be carried out by using other types of laser like the fibre laser and similar results can be achieved if the same amount of input thermal energy was applied. The benefit of this new technique is the ability to apply the laser beam of selected positions on the sample surface and create the texture needed for the interference without damaging or affecting the neighbouring areas. Compared to the traditional method, the insertion is manufactured to a larger diameter than machined to the final interference fit dimensions. This may increase the total cost of the joint due to the usage of high precision machines in addition to the removal of valuable material.

In future work, the process parameters require more optimization and new parameters (e.g. duty cycle) should be investigated to increase the accuracy and extent of process map information. New material might be also investigated based on specific application and

working conditions and the effect of the laser melting can also be examined accordingly. For example, the effect of the laser melting and re-solidification on the corrosion resistance, thermal residual stresses and the presence of microcrack. This was due to a much lower oxidation resistance due to the parameters. Therefore the observation of the microstructure after insertion and removal test had a more worn surface from the pin to the hub specimens. In further research the surface texture geometry and dimensions will be observed under microscopes due to parameter strongly affected the surface textures on the specimen. In the study, the duty cycle can also be investigated together in with other parameters in experiments. This could produce results on the affects of these parameters on the gas flow and hence the oxidation layer on the specimen. Another observation would be the effects on the laser interaction regimes that determine the residual stress and crack formation on the specimens. The study could result on investigations of the laser parameters not only on the oxidation layer but also on the geometry of the melt pool on the specimen. This could be used to produce a unique combination of geometry and residual stresses between the grains. This could result in a combination of crystallographic properties and layer directions on the interferring parts. This will give optimum joint strength characteristics of the specimens. There are numerous factors which affect the insertion and pull-out test. This responses will be considered such as melt pool geometry, dimensions and overlap of the scanning tracks on the specimen. The effect of the process parameters also affects the shielding gas flow that interacts with the melt pool depth. Results of these studies could produce further results on precise control of surface textures due to laser melting process. These tests and many other tests can only be carried out depending on a specific application due to high cost and long time needed.

References

[1] Vladescu, S. *et al*. (2015) 'The effects of surface texture in reciprocating contacts – An experimental study', *Tribology International*, 82, pp. 28–42.

[2] Obeidi, M., McCarthy, E. and Brabazon, D., (2016) 'Methodology of laser processing for precise control of surface micro-topology', *Surface & Coatings Technology*, 307, pp.702–712.

[3] Poprawe, R. (2011) Laser Application Technology, Berlin Heidelberg: Springer.

[4] Aqida, S. (2009) *Thermal Simulation of Laser Surface Modification of H13 Die Steel*, Published PhD thesis. Dublin City University.

[5] Yilbas, B. (2015) 'Laser surface treatment of aluminum based composite mixed with B4C particles', Optics & Laser Technology, 66, pp. 129–137.

[6] Gibson, I. et al. (1997), 'Material properties and fabrication parameters in selective laser sintering process', Rapid Prototyping Journal, 4, (4), pp129-136.

[7] Chandramohan, P. et al. (2017), 'Laser Additive Manufactured Ti–6Al–4V Alloy: Heat Treatment Studies', The Indian Institute of Metals.

[8] Chakraborty, S. and Dutta, P. (2002), 'Numerical Modelling of Heat and Mass Transfer in Laser Surface Alloying: Non-equilibrium Solidification Effects', Materials and Manufacturing Processes, 17, (4), pp. 455-468.

[9] Watanabe, H. and Ishikawa, K. (2009) 'Effect of texture on high temperature deformation behavior at high strain rates in a Mg–3Al–1Zn alloy', Materials Science and Engineering A, 523, pp. 304–311.

[10] Kothandaraman, C. and Rudramoorthy, R. (2007) Fluid Mechanics and Machinery. New Delhi: New Age International Limited Publishers.

[11] Dai, D., (2018) 'Influence of scan strategy and molten pool configuration on microstructures and tensile properties of selective laser melting additive manufactured aluminum based parts', Optics and Laser Technology, 99, pp. 91–100.

[12] SIS (1993) SS-ISO 724: ISO general-purpose metric screw threads-Basic dimensions. SIS 1993. Available at: http://www.sis.se.

[13] Michael. B. (2013) 'Chapter 14 Carbon and Alloy Steels' [PowerPoint], METBD470: Lectures. PSU

[14] Dhahri, M., Frini-Srasra, N. and Srasra, E. (2016) 'The Effect of Preparation Method on Textural and Structural Properties of Alumina-Pillared Interstratified Illite-

Smectite', *Surface Engineering and Applied Electrochemistry*, 52, (6), pp. 524–530.

[15] Klar, E. (2007), Powder Metallurgy Stainless Steels: Processing, Microstructures, and Properties, ASM International. Available at: http://www.asminternational.org.

[16] Steen, W. (1998) Laser material processing, London: Springer-Verlag.

[17] Michael. B. (2013) 'Chapter 14 Carbon and Alloy Steels' [PowerPoint], METBD470: Lectures. PSU.

[18] Furrer, D. and Semiatin, S. (2010) ASM Handbook, Volume 22B, Metals Process Simulation, ASM International (2010), Available at: http://www.asminternational.org.

[19] Vasumathy, D., Meena, A. and Duraiselvam, M. (2017) 'Experimental Study on Evaluating the Effect of Micro Textured Tools in Turning AISI 316 Austenitic Stainless Steel', Procedia Engineering, 184, pp. 50 – 57.

[20] Davim, J. (2013) 'Laser in Manufacturing', John Wiley & Sons, Incorporated.

[21] Aqida, S. et al. (2010), 'Laser Micro-Processing of Amorphous and Partially Crystalline Cu45Zr48Al7 Alloy', Applied Physics A.

[22] Ponce, L. et al. (2005) 'Surface effects in Cu0.64Zn0.36 alloy produced by CO2 laser treatment', Materials Letters, 59, pp. 3909 – 3912.

[23] Shum, P., Zhou, Z. and Li, K. (2014) 'To increase the hydrophobicity, non-stickiness and wear resistance of DLC surface by surface texturing using a laser ablation process', Tribology International, 78, 1–6.

[24] Popescu, A. et al. (2014), Deposition, and surface modification of thin solid structures by high-intensity pulsed laser irradiation, National Institute for Lasers, Plasma and Radiation Physics, Măgurele, Romania.

[25] Kang, M. et al. (2015), 'Micro- and nanoscale surface texturing effects on surface friction', Appl. Surf. Sci., 345, pp. 344–348.

[26] Muhammad, B. (2018) 'Cladding Pumped Thulium-Ytterbium Short Pulse Fiber Lasers', Laser Technology and its Applications , Pakistan: IntechOpen.

[27] Roy, S. et al. (2017), 'Effect of laser treatment parameters on surface modification and tribological behaviour of AISI 8620 steel', Tribology International, 112, pp. 94–102.

[28] Newton, L. (2019), 'Areal topography measurement of metal additive surfaces using focus variation microscopy', *Additive Manufacturing*, 25, pp. 365–389.

[29] Ready, J. (1978) *Industrial Applications of Lasers*, London: Academic Press Inc.

[30] Bartkowska, A. et al. (2015), 'Laser surface modification of boronickelized medium carbon steel', Optics & Laser Technology, 74, pp. 145–157.

[31] Oliveira, G. (1999) ‘Development of an optical scanner to study wear on the working surface of grinding wheels’, Machining Sci. Technol., pp. 239–253.

[32] CEN (2012) ISO 25178-3: Geometrical product specifications - Surface texture: Areal - Part 3: Specification operators. Available at: http://www.iso.org.

[33] Walker, P. and William, H. (2000) CRC handbook of metal etchants, CRC Press LLC.

[34] Subhash, S. et al. (2012), ‘Lasers: Fundamentals, Types, and Operations’, Nanomaterials: Processing and Characterization with Lasers, First Edition.

[35] Spadaro, C., Sunseri, C. and Dispenza, C. (2007) ‘Laser surface treatments for adhesion improvement of aluminium alloys structural joints’, Radiation Physics and Chemistry, 76, (8–9), pp. 1441-1446.

[36] Peng, C. (2017) ‘An Exploratory Investigation of the Mechanical Properties of the Nanostructured Porous Materials Deposited by Laser-Induced Chemical Solution Synthesis’, Journal of Micro- and Nano-Manufacturing, 5, (021007-1).

[37] Obeidi. M. et al. (2018) ‘Laser surface texturing of stainless steel 316L cylindrical pins for interference fit applications’, J. of Materials Processing Tech., 252, pp. 58–68.

[38] Gu, H. (2017) ‘Influences of Energy Density on Porosity and Microstructure of Selective Laser Melted 17- 4PH Stainless Steel’, Solid Freeform Fabrication: Proceedings of the 28th Annual International Solid Freeform Fabrication Symposium: An Additive Manufacturing Conference.

[39] Romano, J. (2018), ‘Triangular laser-induced submicron textures for functionalising stainless steel surfaces’ Published PhD thesis. University of Birmingham.

[40] Chikarakara, E. (2012) Laser Surface Modification of Biomedial Alloys. Published PhD thesis. Dublin City University.

[41] Kumar, C. et al. (2017) ‘Experimental investigation and metallographic characterization of fiber laser beam welding of Ti-6Al-4V alloy using response surface method’, Optics and Lasers in Engineering, 95, pp. 52–68.

[42] Bahce, E. and Ozel, C. (2013), ‘Experimental Investigation of the Effect of Machining Parameters on the Surface Roughness and the Formation of Built Up Edge (BUE) in the Drilling of Al 5005’, Intech: Tribology in Engineering.

[43] Guyson International Limited (2013) Blast Media Data Sheet – Gyson Honite. Available at: http://www.guyson.co.uk.

[44] Zhang, B. et al. (2018), ‘Effects of microstructure on the mechanical properties of a high-strength Ti20Zr6.5Al4V alloy’, Journal of Alloys and Compounds, 735.

[45] Campbell, F. (2010) Understanding the Basics, ProQuest Ebook Central: A S M International.

[46] Suchy, L. (2018) 'Influence of Hub Parameters on Joining Forces and Torque Transmission Output of Plastically-Joined Shaft-Hub-Connections with a Knurled Contact Surface', Machines, 6, (16).

[47] RS PRO (2017) Datasheet: RS Pro 50mm Plain Steel Parallel Dowel Pin, 10mm Diameter RS Stock No: 270-726. Available at: www.rspro.com.

[48] Stamekovic, D., Jovanovic, S. and Milosevic, M. (2001) 'Investigation of the press fit joints by tribology aspect', Facta Universitatis: Mech. Eng., 1, (8), pp. 1057 - 1064.

[49] RS PRO (2017) Datasheet DIN 9021 washer A2, M10 7976254. Available at: www.rspro.com

[50] Cognard, J., Devaux, H. and Sohier, L. (2010) 'Numerical analysis and optimization of cylindrical adhesive joints under tensile loads', International Journal of Adhesion & Adhesives, 30, pp. 706–719.

[51] Troughton, J. (2008) Handbook of Plastics Joining : A Practical Guide, Institute of Welding International.

[52] Ubani, S., Obeidi. M and Brabazon, D. (2019), "Laser surface texturing for the improvement of press-fit joint bond strength" AIP Conference Proceedings, 2113, (150013).

[53] Tada, N. (2017)"Evaluation of Thin Copper Wire and Lead-Free Solder Joint Strength by Pullout Tests and Wire Surface Observation, " Crystals, 7, 255.

[54] Huyuk, H. (2014) 'Analysis of elastic-plastic interference-fit joints', Procedia Engineering, 81, pp. 2030 – 2035.

[55] Wang, H. (2018), 'A model to calculate the laser absorption property of actual surface', International Journal of Heat and Mass Transfer, 118, pp. 562–569.

[56] Oshida, Y. (2013) 11, Surface Modifications, In Bioscience and Bioengineering of Titanium Materials Second Edition, Oxford: Elsevier, pp. 341-456.

[57] Duley, W. (1976), 'CO2 Lasers: Effects and Applications' Academic Press, Inc. London.

[58] Donghua, Dai. et al. (2018), 'Influence of scan strategy and molten pool configuration on microstructures and tensile properties of selective laser melting additive manufactured aluminum based parts', *Optics and Laser Technology*, 99, (2018) 91-100.

[59] Stamekovic, D., Jovanovic, S. and Milosevic, M. (2001), 'Investigation of the press fit joints by tribology aspect' , Facta Universitatis: Mechanical Engineering, 1, (8),

pp 1057 – 1064.

[60] J. Davim, Laser in Manufacturing, John Wiley & Sons, Incorporated, 2013.

[61] J. Ready, Industrial Applications of Lasers, Academic Press Inc. 1978.

Appendix A: Material Preparation

A.1 Design Schematic of Interference Pin and Hub Joint

(dimensions in metres)

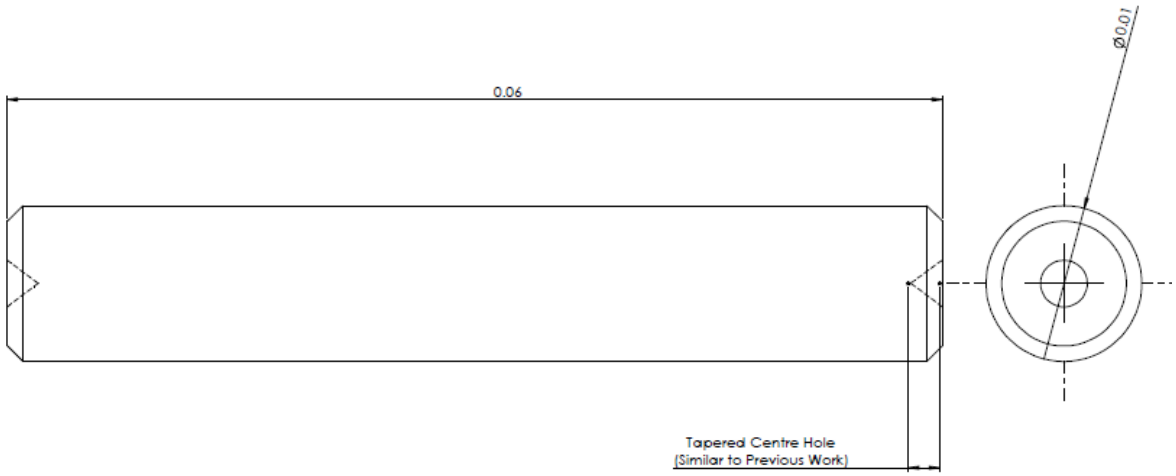

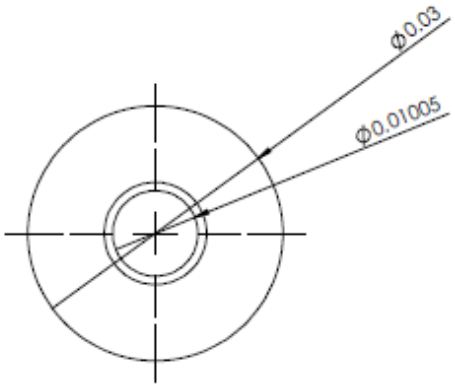

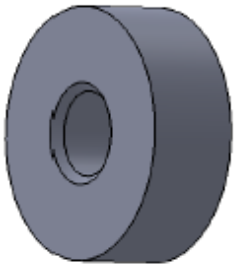

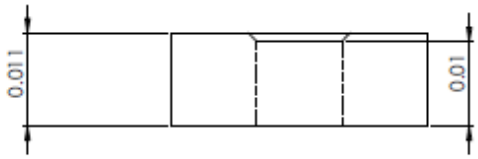

A.2 Manufacturers Specification of Typical Carbon steel rods and Alloy steel Hubs

Datasheet

ENGLISH

DIN 9021 washer A2, M10

7976254

Dimensions:

Finish	Plain
For Screw/Bolt Size	M10
Inside Diameter	10.5 mm
Material	Stainless Steel
Finish	Plain
Outside Diameter	30 mm
Stainless Steel Type	A2
Thickness	2.5 mm

ENGLISH

Datasheet

RS Pro 50mm Plain Steel Parallel Dowel Pin, 10mm Diameter

RS Stock No: **270-726**

Product Details

RS Pro parallel dowel pin made of case hardened mild steel is plain finished for an improved toughness and hardness. The pin is highly corrosion resistant and is used to retain parts in a fixed position, maintain alignment between different parts or to join different components together. It measures 50 mm long with a diameter of 10 mm.

Features and Benefits

- Case hardened mild steel construction
- Comes in plain finish
- To BS/ISO 8734 limits. Type B

A.3 Sandblasting Media Specifications

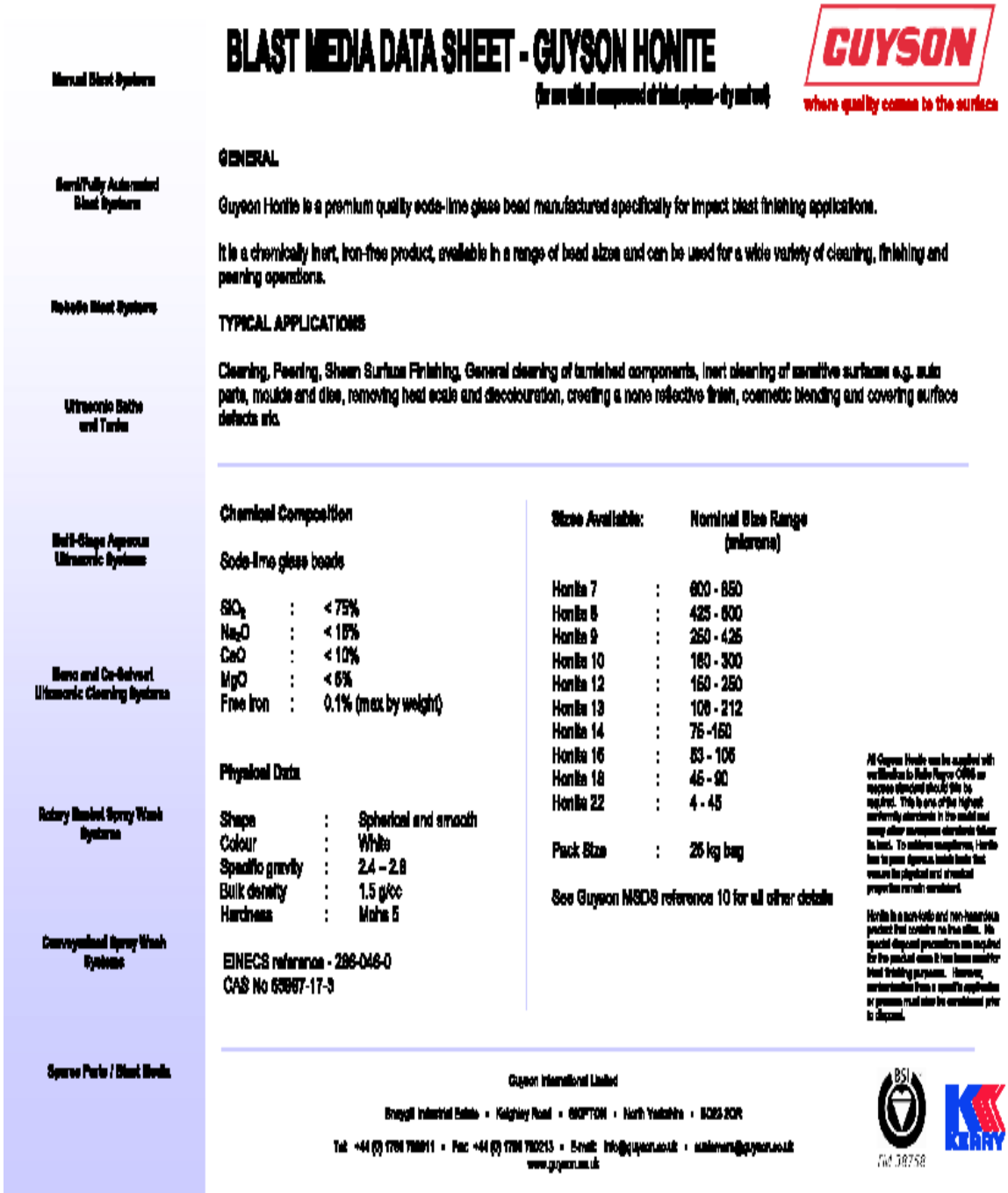

Manual Blast Systems

Semi/Fully Automated Blast Systems

Robotic Blast Systems

Ultrasonic Baths and Tanks

Bell-Glaze Aqueous Ultrasonic Systems

Nano and Co-Solvent Ultrasonic Cleaning Systems

Rotary Basket Spray Wash Systems

Conveyorised Spray Wash Systems

Spares Parts / Blast Media

BLAST MEDIA DATA SHEET - GUYSON HONITE

(for use with all compressed air blast systems - dry and wet)

GUYSON

where quality comes to the surface

GENERAL

Guyson Honite is a premium quality soda-lime glass bead manufactured specifically for impact blast finishing applications.

It is a chemically inert, iron-free product, available in a range of bead sizes and can be used for a wide variety of cleaning, finishing and peening operations.

TYPICAL APPLICATIONS

Cleaning, Peening, Sheen Surface Finishing, General cleaning of tarnished components, inert cleaning of sensitive surfaces e.g. auto parts, moulds and dies, removing heat scale and discolouration, creating a none reflective finish, cosmetic blending and covering surface defects etc.

Chemical Composition

Soda-lime glass beads

SiO_2	:	< 75%
Na_2O	:	< 18%
CaO	:	< 10%
MgO	:	< 6%
Free iron	:	0.1% (max by weight)

Physical Data

Shape	:	Spherical and smooth
Colour	:	White
Specific gravity	:	2.4 – 2.8
Bulk density	:	1.5 g/cc
Hardness	:	Mohs 5

EINECS reference - 266-046-0
CAS No 65997-17-3

Sizes Available:		Nominal Size Range (microns)
Honite 7	:	600 - 850
Honite 8	:	425 - 600
Honite 9	:	250 - 425
Honite 10	:	180 - 300
Honite 12	:	150 - 250
Honite 13	:	106 - 212
Honite 14	:	75 -150
Honite 16	:	53 - 106
Honite 18	:	45 - 90
Honite 22	:	4 - 45
Pack Size	:	25 kg bag

See Guyson MSDS reference 10 for all other details

All Guyson Honite can be supplied with certification to Rolls Royce CW6 or equivalent should this be required. This is one of the highest commonly standards in the shot and many other aerospace standards follow its lead. To achieve compliance, Honite has to pass rigorous tests that ensure its physical and chemical properties remain consistent.

Honite is a non-toxic and non-hazardous product that contains no free silica. No special disposal procedures are required for the product when it has been used for blast finishing purposes. However, contamination from a specific application or process must also be considered prior to disposal.

Guyson International Limited

Bracyll Industrial Estate • Keighley Road • SKIPTON • North Yorkshire • BD23 2QR

Tel: +44 (0) 1756 799911 • Fax: +44 (0) 1756 792213 • Email: info@guyson.co.uk • sales@guyson.co.uk

www.guyson.co.uk

FM 38758

Appendix B: Factorial Design of Specimen

B.1 Factors for Response Surface Model of Parameters

Power (W)	F.P (mm)	O.V (%)
300	0	20
300	1.5	20
300	1.5	-20
400	1.5	-20
300	0	0
300	-1.5	-20
500	1.5	20
300	-1.5	20
400	-1.5	0
400	-1.5	-20
500	1.5	-20
400	1.5	20
400	0	20
500	-1.5	20
500	0	0
400	0	0
500	0	-20
300	-1.5	0
400	1.5	0
500	1.5	0
500	-1.5	-20
500	-1.5	0
400	0	-20
400	-1.5	20
300	0	-20
300	1.5	0
500	0	20

B.2 ANOVA Models of Diameter Increase

Response 2 Diameter Increase

ANOVA for Response Surface Cubic model (Aliased)

Analysis of variance table [Partial sum of squares - Type III]

Source	Sum of Squares	df	Mean Square	F Value	p-value Prob > F	
Model	7.34	16	0.46	0.97	0.5418	not significant
A-POWER	*0.72*	*1*	*0.72*	*1.51*	*0.2473*	
B-F.P	*0.71*	*1*	*0.71*	*1.49*	*0.2506*	
C-OV	*0.069*	*1*	*0.069*	*0.14*	*0.7121*	
AB	*0.89*	*1*	*0.89*	*1.87*	*0.2013*	
AC	*0.039*	*1*	*0.039*	*0.082*	*0.7806*	
BC	*3.008E-003*	*1*	*3.008E-003*	*6.329E-003*	*0.9382*	
A^2	*0.097*	*1*	*0.097*	*0.20*	*0.6604*	
B^2	*0.12*	*1*	*0.12*	*0.25*	*0.6252*	
C^2	*0.64*	*1*	*0.64*	*1.35*	*0.2715*	
ABC	*0.021*	*1*	*0.021*	*0.044*	*0.8377*	
A^2B	*0.11*	*1*	*0.11*	*0.23*	*0.6436*	
A^2C	*0.61*	*1*	*0.61*	*1.29*	*0.2820*	
AB^2	*0.36*	*1*	*0.36*	*0.75*	*0.4054*	
AC^2	*1.66*	*1*	*1.66*	*3.50*	*0.0910*	
B^2C	*0.074*	*1*	*0.074*	*0.16*	*0.7007*	
BC^2	*1.07*	*1*	*1.07*	*2.26*	*0.1638*	
A^3	*0.000*	*0*				
B^3	*0.000*	*0*				
C^3	*0.000*	*0*				
Residual	4.75	10	0.48			
Cor Total	12.09	26				

The Model F-value of 0.97 implies the model is not significant relative to the noise. There is a 54.18 % chance that a F-value this large could occur due to noise.

Values of "Prob > F" less than 0.0500 indicate model terms are significant.
In this case there are no significant model terms.
Values greater than 0.1000 indicate the model terms are not significant.
If there are many insignificant model terms (not counting those required to support hierarchy), model reduction may improve your model.

Std. Dev.	0.69	R-Squared	0.6070
Mean	10.28	Adj R-Squar	-0.0218
C.V. %	6.71	Pred R-Squa	-2.9991
PRESS	48.37	Adeq Precisi	4.948
-2 Log Likelih	29.72	BIC	85.75
		AICc	131.72

B.3 ANOVA Model of Surface Roughness

Response 3 Surface Roughness

ANOVA for Response Surface Cubic model (Aliased)

Analysis of variance table [Partial sum of squares - Type III]

Source	Sum of Squares	df	Mean Square	F Value	p-value Prob > F	
Model	7398.89	16	462.43	0.96	0.5472	not significant
A-POWER	*92.15*	*1*	*92.15*	*0.19*	*0.6715*	
B-F.P	*1029.72*	*1*	*1029.72*	*2.13*	*0.1749*	
C-OV	*813.61*	*1*	*813.61*	*1.69*	*0.2234*	
AB	*2686.01*	*1*	*2686.01*	*5.56*	*0.0400*	
AC	*68.26*	*1*	*68.26*	*0.14*	*0.7147*	
BC	*225.67*	*1*	*225.67*	*0.47*	*0.5097*	
A^2	*91.40*	*1*	*91.40*	*0.19*	*0.6727*	
B^2	*451.34*	*1*	*451.34*	*0.93*	*0.3564*	
C^2	*136.53*	*1*	*136.53*	*0.28*	*0.6065*	
ABC	*409.59*	*1*	*409.59*	*0.85*	*0.3787*	
A^2B	*489.13*	*1*	*489.13*	*1.01*	*0.3379*	
A^2C	*22.75*	*1*	*22.75*	*0.047*	*0.8325*	
AB^2	*117.54*	*1*	*117.54*	*0.24*	*0.6324*	
AC^2	*158.16*	*1*	*158.16*	*0.33*	*0.5797*	
B^2C	*271.55*	*1*	*271.55*	*0.56*	*0.4705*	
BC^2	*108.32*	*1*	*108.32*	*0.22*	*0.6459*	
A^3	*0.000*	*0*				
B^3	*0.000*	*0*				
C^3	*0.000*	*0*				
Residual	4827.78	10	482.78			
Cor Total	12226.67	26				

The Model F-value of 0.96 implies the model is not significant relative to the noise. There is a 54.72 % chance that a F-value this large could occur due to noise.

Values of "Prob > F" less than 0.0500 indicate model terms are significant.
In this case AB is a significant model term.
Values greater than 0.1000 indicate the model terms are not significant.
If there are many insignificant model terms (not counting those required to support hierarchy), model reduction may improve your model.

Std. Dev.	21.97	R-Squared	0.6051
Mean	66.78	Adj R-Squar	-0.0266
C.V. %	32.90	Pred R-Squa	-2.1546
PRESS	38570.56	Adeq Precisi	3.308
-2 Log Likelih	216.65	BIC	272.68
		AICc	318.65

B.4 Input Parameters

Input Parameters											C.I = 95%			α =0.05	
Sample No.	P (W)	zf (mm)	O.V (%)	I_o (kW/m	N (rpm	vt (mm/min	vf (mm/	vs (mm/m	T	Duty Cycle	D1 (mm)	D2 (mm)	D3 (mm)	D_{avg} (mm)	σ_{avg} (mm)
1	500	-1.5	-20	1486	48	1500	11.5	1500	2117	50	0.0106	0.0107	0.0108	0.0107	0.00008
2	500	0	20	1483	32	1000	5.1	1000	1102	50	0.0106	0.0108	0.0108	0.0107	0.00012
3	400	1.5	20	1252	32	1000	5.1	1000	1147	50	0.0101	0.0102	0.0102	0.0102	0.00006
4	500	0	0	1474	38	1200	7.6	1200	1451	50	0.0108	0.0107	0.0109	0.0108	0.00010
5	300	0	0	914	38	1200	7.6	1200	1490	50	0.0104	0.0105	0.0104	0.0104	0.00005
6	500	1.5	0	1539	38	1200	7.6	1200	1502	50	0.0104	0.0103	0.0103	0.0103	0.00005
7	400	-1.5	-20	1215	48	1500	11.5	1500	2157	50	0.0106	0.0105	0.0104	0.0105	0.00010
8	300	0	-20	916	48	1500	11.5	1500	2168	50	0.0106	0.0104	0.0103	0.0104	0.00016
9	400	-1.5	0	1238	38	1200	7.6	1200	1509	50	0.0103	0.0103	0.0103	0.0103	0.00001
10	400	1.5	0	1221	38	1200	7.6	1200	1492	50	0.0104	0.0105	0.0104	0.0104	0.00007
11	300	-1.5	0	924	38	1200	7.6	1200	1503	50	0.0103	0.0103	0.0104	0.0103	0.00006
12	300	1.5	-20	945	48	1500	11.5	1500	2227	50	0.0101	0.0101	0.0101	0.0101	0.00000
13	500	1.5	-20	1562	48	1500	11.5	1500	2211	50	0.0103	0.0102	0.0101	0.0102	0.00008
14	500	1.5	20	1517	32	1000	5.1	1000	1120	50	0.0105	0.0105	0.0105	0.0105	0.00001
15	400	0	20	1220	32	1000	5.1	1000	1125	50	0.0105	0.0104	0.0104	0.0104	0.00006
16	400	0	0	1233	38	1200	7.6	1200	1504	50	0.0102	0.0104	0.0104	0.0103	0.00011
17	400	1.5	-20	1257	48	1500	11.5	1500	2222	50	0.0102	0.0101	0.0101	0.0101	0.00005
18	500	-1.5	20	1487	32	1000	5.1	1000	1104	50	0.0107	0.0109	0.0105	0.0107	0.00020
19	400	0	-20	1213	48	1500	11.5	1500	2154	50	0.0105	0.0106	0.0104	0.0105	0.00010
20	300	-1.5	-20	925	48	1500	11.5	1500	2186	50	0.0103	0.0104	0.0103	0.0103	0.00003
21	300	0	20	916	32	1000	5.1	1000	1126	50	0.0105	0.0104	0.0104	0.0104	0.00003
22	500	-1.5	0	1512	38	1200	7.6	1200	1481	50	0.0002	0.0104	0.0105	0.0070	0.00593
23	400	-1.5	20	1209	32	1000	5.1	1000	1117	50	0.0105	0.0105	0.0106	0.0105	0.00006
24	300	1.5	20	945	32	1000	5.1	1000	1153	50	0.0101	0.0101	0.0101	0.0101	0.00000
25	300	1.5	0	951	38	1200	7.6	1200	1538	50	0.0100	0.0100	0.0100	0.0100	0.00000
26	300	-1.5	20	909	32	1000	5.1	1000	1120	50	0.0106	0.0104	0.0105	0.0105	0.00010
27	500	0	-20	1510	48	1500	11.5	1500	290	50	0.0108	0.0106	0.0102	0.0105	0.00033
Max.	500	1.50	20.0	1562	47.75	1500	11.46	1500	2227	50.0	0.0108	0.0109	0.0109	0.0108	0.00593
Min.	300	-1.50	-20.0	909	31.83	1000	5.09	1000	290	50.0	0.0002	0.0100	0.0100	0.0070	0.00000
Avg.	400	0.00	0.0	1222	39.29	1234	8.08	1235	1512	50.0	0.0097	0.0104	0.0104	0.0102	0.00048
Std. Dev.	83	1.25	16.6	245	6.65	209	2.66	209	540	0.0	0.0026	0.0002	0.0002	0.0009	0.00148

Gas and Material Parameters for Laser Processing							t-Test: Two-Sample Assuming Equal Variances for Measured Parameters								
Gas Parameters		Laser Parameters		Material Parameter				P (W)	F.P (mm)	O.V (%)	D (mm)	P (W)	F.P (mm)	O.V (%)	Ra (µm)
Gas	N_2	Laser	CO_2	Materia	Mild Steel EH		Mean	400	0	0	0	400	0	0	13
T (°K)	293	λ (µm)	10.6	E_{tube} (N	2.07E+11		Variance	6923	2	277	0	6923	2	277	151
Q (L/s)	0.05	τ (ms)	50	v_{tube}	0.3		Observa	27	27	27	27	27	27	27	27
ρ (kg/m	1.35kg/m	p (MPa)	0.2	ρ (kg/m	7900		df	52	52	52		52	52	52	
p_{atm}	101300 P	P_{avg} (kW	1.5	T_m (K)	1744		t Stat	25	0	0		24	-6	-3	
c_p (J/kg	1042	f (Hz)	628	κ (W/M	45		P(T<=t)	0	0	0		0	0	0	
v_p (m/s	388m/s	d (mm)	0.2	α_{tube} (1	6.00E-06		t Critical	1.67	1.67	1.67		1.67	1.67	1.67	
z (m)	0.6m	PRF (Hz)	100	κ (m^2/s	4.00E-07		P(T<=t)	0	1	1		0	0	0	
p (MPa)	0.2026	f (m)	0.125	α (°)	45		t Critical	2.007	2.007	2.007		2.007	2.007	2.007	

Correlation Coefficient, r			
Surface	P (W)	F.P (mm	O.V (%)
Ed (J/m	0.095	-0.277	0.163
T (°K)	-0.0581	0.2208	-0.1928
D (mm)	0.5366	-0.551	0.15732
Ra (µm	0.1163	0.3114	0.28106
Fa (kN)	0.3126	-0.523	0.16764
Fn (kN)	0.0903	-0.12	0.03432
* F (kN)	0.3617	-0.189	0.08342

B.5 Measured Parameters

Measured Parameters			C.I = 95%							α = 0.05	
Sample No.	τ (ms)	ε (mm/mm)	FL1(kN)	FL2(kN)	Ra1 (mm)	Ra2 (mm)	Ra (µm)	RSm1 (m	RSm2 (mn	Str	c
1	8.06	0.0000179	29428	5800	382	480	6.2	221	261	1.73	1.84
2	12.00	0.0000218	18980	2807	430	448	15.0	236	251	1.82	1.78
3	12.10	0.0000219	914	1546	474	473	66.9	256	283	1.85	1.67
4	10.00	0.0000199	26812	3372	450	474	13.4	237	254	1.90	1.87
5	10.00	0.0000199	10016	5281	464	418	9.1	251	223	1.85	1.87
6	10.08	0.0000200	3523	1134	450	497	9.8	236	267	1.91	1.86
7	8.06	0.0000179	4242	902	495	483	20.0	265	254	1.87	1.90
8	8.00	0.0000178	5470	1122	486	427	8.4	261	259	1.86	1.65
9	10.08	0.0000200	5250	2568	405	540	5.8	217	288	1.86	1.87
10	10.08	0.0000200	2142	795	463	481	15.6	260	264	1.78	1.82
11	10.08	0.0000200	6479	3536	499	533	12.5	274	305	1.82	1.75
12	8.06	0.0000179	0	427	523	435	7.3	254	244	2.06	1.79
13	8.06	0.0000179	0	1473	477	398	7.0	261	231	1.83	1.72
14	12.10	0.0000219	3012	2316	394	390	28.1	220	218	1.79	1.79
15	12.00	0.0000218	14501	147	430	440	19.0	233	248	1.85	1.77
16	10.00	0.0000199	2303	442	452	459	23.8	239	247	1.89	1.86
17	8.06	0.0000179	2567	3497	537	505	13.0	288	271	1.86	1.86
18	12.10	0.0000219	7610	2376	374	608	4.7	210	383	1.79	1.59
19	8.00	0.0000178	5078	2048	487	384	6.1	254	218	1.92	1.76
20	8.06	0.0000179	5187	506	520	416	6.5	265	240	1.96	1.74
21	12.00	0.0000218	1752	7810	396	430	9.9	219	237	1.81	1.82
22	10.08	0.0000200	12480	1343	386	475	6.5	223	258	1.73	1.84
23	12.10	0.0000219	18692	2024	403	498	6.6	226	292	1.78	1.70
24	12.10	0.0000219	5331	2851	784	483	5.3	277	270	2.83	1.79
25	10.08	0.0000200	0	0	771	567	6.7	280	260	2.75	2.18
26	12.10	0.0000219	22240	0	466	406	8.0	243	260	1.92	1.56
27	8.00	0.0000178	10893	4673	457	479	14.1	235	222	1.95	2.15
Max.	12.10	2.19166E-05	29428	7810	784	608	66.9	288	383	2.83	2.18
Min.	8.00	1.78238E-05	0	0	374	384	4.7	210	218	1.73	1.56
Avg.	10.05	1.99101E-05	8770	2366	483	470	14.7	246	262	1.95	1.81
Std. Dev.	1.67	1.67206E-06	8921	2134	110	59	15.3	23	40	0.30	0.15

t-Test: Two-Sample Assuming Equal Variances of Output Parameters

	P (W)	F.P (mm)	O.V (%)	Fa (kN)	Fn (kN)
Mean	400	0	0	19628	8330
Variance	6923	2	277	267930520	69199923
Observation	27	27	27	27	27
df	52	52	52		
t Stat	-6	-6	-6		
P(T<=t) one-	0	0	0		
t Critical one	1.67	1.67	1.67		
P(T<=t) two-	0	0	0		
t Critical two	2.007	2.007	2.007		

B.6 Calculated Parameters

Calculated Parameters			C.I = 95%		α = 0.05	
Sample No.	FΣline,max	H (m)	R_{eL}(MPa)	R_m (MPa)	D_z (mm)	w(z) (mm)
1	958	0.00024	116	338.30	32.5	0.202
2	31219	0.00016	59	217.30	32.3	0.200
3	14027	0.00016	6	11.69	32.5	0.202
4	5490	0.00020	81	303.13	32.3	0.200
5	6393	0.00020	54	121.17	32.3	0.200
6	4117	0.00020	31	43.53	32.5	0.202
7	1597	0.00024	34	50.97	32.5	0.202
8	958	0.00024	41	66.52	32.3	0.200
9	8524	0.00020	34	65.56	32.5	0.202
10	5490	0.00020	17	26.02	32.5	0.202
11	6862	0.00020	28	80.16	32.5	0.202
12	1278	0.00024	0	0.00	32.5	0.202
13	1278	0.00024	17	0.00	32.5	0.202
14	52031	0.00016	48	36.12	32.5	0.202
15	36301	0.00016	22	175.88	32.3	0.200
16	8524	0.00020	20	28.52	32.3	0.200
17	718	0.00024	27	33.09	32.5	0.202
18	21781	0.00016	18	87.71	32.5	0.202
19	891	0.00024	34	60.79	32.3	0.200
20	1114	0.00024	22	64.35	32.5	0.202
21	23379	0.00016	66	21.30	32.3	0.200
22	10655	0.00020	53	148.70	32.5	0.202
23	18703	0.00016	33	222.42	32.5	0.202
24	41625	0.00016	61	69.11	32.5	0.202
25	4117	0.00020	0	0.00	32.5	0.202
26	53722.0	0.00016	41	266.36	32.5	0.202
27	53288.0	0.00024	72	129.41	32.3	0.200
Max.	53722	0.000	116.0	338	32.5	0.202
Min.	718	0.000	0.0	0.000	32.3	0.200
Avg.	16189	0.000	39.7	103.7	32.4	0.201
Std. Dev.	18348	3.32E-05	29.5	102.7	0.0951	7.58E-04

t-Test of Calculated Parameters for Calculated Parameters						
	P (W)	F.P (mm)	O.V (%)	Ed (J/mm³)	T (°K)	
Mean	400	0	0	1480	183	
Variance	6923	2	277	311903	5899	
Observation	27	27	27	31	31	
df	52	56	52			
t Stat	-12	-14	-16			
P(T<=t) one-	0	0	0			
t Critical one	1.67	1.67	1.67			
P(T<=t) two-	0	0	0			
t Critical two	2.007	2.003	2.007			

B.7 Output Parameters

Output Parameters				C.I = 95%			α = 0.05	
Sample No.	V (m^3)	$A_{s,nom}$ (mm^2)	k (N/N)	F (kN)	σw (MPa	Ed (J/mm	t (s)	ε (mm)
1	0.000343	87.0	0.20	61636	3924	144	0.105	0.07
2	0.000083	87.3	0.15	39619	3927	324	0.236	0.07
3	0.000523	78.2	1.69	4278	3924	259	0.236	0.02
4	0.000106	88.5	0.13	57158	3927	225	0.157	0.08
5	0.000696	82.7	0.53	28378	3927	135	0.157	0.04
6	0.000091	80.9	0.32	8834	3924	225	0.157	0.03
7	0.000058	83.2	0.21	9636	3924	115	0.105	0.05
8	0.000069	82.2	0.21	12028	3927	86	0.105	0.04
9	0.000314	80.1	0.49	14602	3924	180	0.157	0.03
10	0.000074	82.3	0.37	5268	3924	180	0.157	0.04
11	0.000482	80.8	0.55	17994	3924	135	0.157	0.03
12	0.000000	77.1	0.00	762	3924	86	0.105	0.01
13	0.000000	78.5	0.00	2540	3924	144	0.105	0.02
14	0.000356	83.4	0.77	9534	3924	324	0.236	0.05
15	0.000000	82.4	0.01	27054	3927	259	0.236	0.04
16	0.000021	80.7	0.19	5176	3927	180	0.157	0.03
17	0.001429	77.6	1.36	11302	3924	115	0.105	0.01
18	0.000148	86.8	0.31	17361	3924	324	0.236	0.07
19	0.000248	83.5	0.40	13358	3927	115	0.105	0.05
20	0.000015	80.6	0.10	11059	3924	86	0.105	0.03
21	0.006964	82.2	4.46	17359	3927	194	0.236	0.04
22	0.000036	83.9	0.11	24100	3924	225	0.157	0.05
23	0.000044	84.0	0.11	36714	3924	259	0.236	0.05
24	0.000305	77.1	0.53	20214	3924	194	0.236	0.01
25	0.000000	76.2	0.00	0	3924	135	0.157	0.00
26	0.000000	83.5	0.00	42739	3924	194	0.236	0.05
27	0.000601	-0.1	0.43	31252	3927	144	0.105	-0.05
Max.	0.007	88.5	4.459	61636	3927	324	0.236	0.0800
Min.	0.000	-0.1	0.000	0	3924	86	0.105	-0.0540
Avg.	0.001	76.5	0.623	20400	3925	186	0.166	0.0351
Std. Dev.	0.001734006	21.1	1.11	17713	1	75	0.0547	0.0317

t-Test: Two-Sample Assuming Equal Variances of Output Parameters

	P (W)	F.P (mm)	O.V (%)	F (kN)
Mean	400	0	0	2252
Variance	6923	2	277	3710608
Observations	27	27	27	27
df	52	52	52	
t Stat	-5	-6	-6	
P(T<=t) one-	0	0	0	
t Critical one	1.67	1.67	1.67	
P(T<=t) two-	0	0	0	
t Critical two	2.007	2.007	2.007	

Appendix C: Specimen Testing Specifications

C.1 Testing Methods

ISO 898-1:2009(E)

Table 7 — Proof loads — ISO metric fine pitch thread

Thread $d \times P$	Nominal stress area $A_{s,nom}$ [a] mm²	Property class								
		4.6	4.8	5.6	5.8	6.8	8.8	9.8	10.9	12.9(12.9
		Proof load, F_p ($A_{s,nom} \times S_{p,nom}$), N								
M8 × 1	39,2	8 820	12 200	11 000	14 900	17 200	22 700	25 500	32 500	38 000
M10 × 1,25	61,2	13 800	19 000	17 100	23 300	26 900	35 500	39 800	50 800	59 400
M10 × 1	64,5	14 500	20 000	18 100	24 500	28 400	37 400	41 900	53 500	62 700
M12 × 1,5	88,1	19 800	27 300	24 700	33 500	38 800	51 100	57 300	73 100	85 500
M12 × 1,25	92,1	20 700	28 600	25 800	35 000	40 500	53 400	59 900	76 400	89 300
M14 × 1,5	125	28 100	38 800	35 000	47 500	55 000	72 500	81 200	104 000	121 000
M16 × 1,5	167	37 600	51 800	46 800	63 500	73 500	96 900	109 000	139 000	162 000
M18 × 1,5	216	48 600	67 000	60 500	82 100	95 000	130 000	—	179 000	210 000
M20 × 1,5	272	61 200	84 300	76 200	103 000	120 000	163 000	—	226 000	264 000
M22 × 1,5	333	74 900	103 000	93 200	126 000	146 000	200 000	—	276 000	323 000
M24 × 2	384	86 400	119 000	108 000	146 000	169 000	230 000	—	319 000	372 000
M27 × 2	496	112 000	154 000	139 000	188 000	218 000	298 000	—	412 000	481 000
M30 × 2	621	140 000	192 000	174 000	236 000	273 000	373 000	—	515 000	602 000
M33 × 2	761	171 000	236 000	213 000	289 000	335 000	457 000	—	632 000	738 000
M36 × 3	865	195 000	268 000	242 000	329 000	381 000	519 000	—	718 000	839 000
M39 × 3	1 030	232 000	319 000	288 000	391 000	453 000	618 000	—	855 000	999 000

[a] To calculate $A_{s,nom}$, see 9.1.6.1.

8 Applicability of test methods

8.1 General

Two main groups of test series are established for testing the mechanical and physical properties of fasteners specified in Table 3, FF and MP. Whereas group FF is used for testing finished fasteners, group MP is used for testing material properties of the fasteners. The two groups are divided into test series FF1, FF2, FF3, FF4 and MP1 and MP2, respectively, for different types of fasteners. However, not all mechanical and physical properties specified in Table 3 can be tested on all types or sizes of fasteners due primarily to dimensional and/or loadability reasons.

8.2 Loadability of fasteners

8.2.1 Fasteners with full loadability

A fastener with full loadability is a finished fastener, standardized or non-standardized, which, when tensile tested according to the test series FF1, FF2 or MP2,

a) breaks in the free threaded length for fasteners with $d_s > d_2$

or

breaks in the free threaded length or in the unthreaded shank for fasteners with $d_s \approx d_2$, and

b) meets the minimum ultimate tensile load, $F_{m\,min}$, according to Tables 4 or 6.

C.2 Testing Apparatus Method and Specification

9.3.3 Apparatus

The tensile testing machine shall be in accordance with ISO 7500-1. Side thrust on the fastener shall be avoided e.g. by self-aligning grips.

9.3.4 Testing device

The grips and the adaptors shall be as follows:

— hardness of 45 HRC min;

— hole diameter, d_h, according to Table 15;

— thread tolerance class of the internally threaded adaptor(s) according to Table 14.

The testing device should be sufficiently rigid to avoid deformation that could influence the determination of the load at 0,0048 d non-proportional elongation, F_{pf}, or of the elongation after fracture, A_f.

9.3.5 Test procedure

The fastener shall be tested as received.

Mount the fastener to be tested into adaptors as shown in Figure 2 a) and b); mount the studs to be tested into two threaded adaptors as shown in Figure 2 c) and d). The length of thread engagement shall be at least 1 d.

The free threaded length, l_{th}, subjected to the load shall be 1,2 d.

NOTE To obtain l_{th} = 1,2 d in a practical way, the following procedure is proposed: first, screw on the threaded adaptor up to the thread run-out; then unscrew the adaptor by the required number of turns corresponding to l_{th} = 1,2 d.

The tensile test shall be carried out in accordance with ISO 6892-1. The speed of testing, as determined with a free running cross head, shall not exceed 10 mm/min up to the load at 0,0048 d non-proportional elongation, F_{pf}, and 25 mm/min beyond.

Measure the load, F, continuously until fracture occurs, either directly, by means of an adequate electronic device (e.g. microprocessor), or on the curve of load against displacement, see ISO 6892-1; the curve can be plotted either automatically or graphically.

For acceptable accurate graphical measurement, the scale of the curve shall be such that the elastic slope (straight part of the curve) lies between 30° and 45° against the load axis.

9.3.6 Test results

9.3.6.1 Determination of the elongation after fracture, A_f

9.3.6.1.1 Method

The plastic elongation, ΔL_p, is measured directly on the load-displacement curve, plotted either electronically or graphically, see Figure 3.

C.3 Test Specimens Specifications

b) machined test pieces made from studs:

- 3 mm $\leqslant d \leqslant$ 39 mm;
- thread length $b \geqslant 1\,d$;
- thread length of the stud (metal) end $b_m \geqslant 1\,d$;
- total length $l_t \geqslant 6\,d_0 + 2\,r + 2\,d$ (as indicated in Figure 6) to determine A;
- total length $l_t \geqslant 4\,d_0 + 2\,r + 2\,d$ (as indicated in Figure 6) to determine Z.

c) property classes 4.6, 5.6, 8.8, 9.8, 10.9 and 12.9/12.9.

NOTE Machined test pieces made from bolts and screws can also be made from fasteners which, due to their geometry, have reduced loadability, provided that the head is stronger than the cross-sectional area, S_o, of the test piece, and also of fasteners with unthreaded shank diameter $d_s < d_2$ (see 8.2).

Fasteners in property classes 4.8, 5.8 and 6.8 (work-hardened fasteners) shall be tensile tested full-size, see 9.3.

9.7.3 Apparatus

The tensile testing machine shall be in accordance with ISO 7500-1. Side thrust on the fastener shall be avoided, e.g. by self-aligning grips.

9.7.4 Testing device

The grips and the adaptors shall be as follows:

- hardness of 45 HRC min;
- hole diameter, d_h, according to Table 15;
- thread tolerance class of the internally threaded adaptor(s) according to Table 14.

9.7.5 Machined test pieces

The test piece shall be machined from the fastener as received. The test piece shown in Figure 6 shall be used for the tensile test.

The diameter of the machined test piece shall be $d_0 < d_{3\,min}$, but whenever possible $d_0 \geqslant 3$ mm.

When machining the test pieces of quenched and tempered fasteners with nominal diameter $d > 16$ mm the reduction of the original diameter, d, shall not exceed 25 % (about 44 % of the initial cross-sectional area). For test pieces made from studs, both ends shall have a thread length of minimum 1 d.

9.7.6 Test procedure

The tensile test shall be carried out in accordance with ISO 6892-1. The speed of testing, as determined with a free running cross head, shall not exceed 10 mm/min up to the load at lower yield strength, R_{eL}, or the load at the stress at 0,2 % non-proportional elongation, $R_{p0,2}$, and 25 mm/min beyond.

The tensile test shall be continued until fracture occurs.

Measure the ultimate tensile load, F_m.